Influence of upstream turbulence on flow past a confined circular cylinder

Wilson Lu, Leon Chan, and Andrew Ooi*
Department of Mechanical Engineering, The University of Melbourne, Parkville 3010, Victoria, Australia

(Received 12 February 2025; accepted 22 April 2026; published 1 June 2026)

In this paper, numerical simulations are conducted of flow past a circular cylinder confined symmetrically in a channel. The effects of upstream turbulence on wake properties are studied with upstream conditions assumed to be a canonical turbulent channel flow. Simulations have been conducted at blockages of $\beta = 0.3$, 0.5, and 0.7, where blockage is defined as the ratio of cylinder diameter to channel height. It is found for the lowest blockage, $\beta = 0.3$, turbulence trips the shear layers separating off the cylinder, forming Kelvin-Helmholtz vortices which rapidly roll-up and form Kármán vortices further downstream. This mechanism prevents merging of Kelvin-Helmholtz vortices, evidenced by a lack of a subharmonic peak in spectra of probes placed in the shear layer. For $\beta = 0.5$, acceleration of fluid through the gap between the cylinder and channel wall partially relaminarizes the flow, reducing turbulence. Despite this, the surviving turbulence still trips the cylinder shear layer, causing it to break down. Finally, for $\beta = 0.7$, a large change in wake dynamics is found to occur. Relaminarization again occurs through the gap, but is insufficient to suppress all turbulence. Hence, tripping the cylinder shear layer and breaking it down before wake bias could occur. This therefore results in the time- and spanwise-averaged flow being symmetric, unlike its laminar upstream counterpart. Spectral analysis also finds a strong subharmonic peak, indicating merging of Kelvin-Helmholtz vortices for $\beta = 0.5$ and 0.7.

DOI: 10.1103/grbb-q47x

I. INTRODUCTION

Flow past a circular cylinder is typically considered a prototype problem for bluff body flows that may be encountered in physical scenarios, including buildings, vortex-induced vibration (VIV) energy converters [1], and wind turbines. As such, an extensive body of research exists on flow properties within both laminar and turbulent regimes (see for example the reviews of Williamson [2] and Derakhshandeh and Alam [3]). At sufficiently high Reynolds numbers, still within the laminar regime, periodic shedding of vortices occurs forming a Kármán vortex street [2]. When the Reynolds number is further increased into the subcritical regime, transition to turbulence occurs within the shear layers separating from the cylinder via a Kelvin-Helmholtz mechanism [4–7]. However, in the work considered thus far, the flow has been idealized through assumption that incoming flow to the cylinder is purely laminar, a condition seldom realized in engineering scenarios. This has therefore led to considerations of perturbing the upstream flow and studying its effects on wake properties. The simplest method is through addition of harmonic perturbations to the inflow with some excitation frequency f_e. Resonance, or lock-on in the literature, occurs when the excitation frequency is close to the shedding frequency and results in a coupling over a band of excitation frequencies [8,9]. Within this regime Konstantinidis and Liang [9] observed a number of changes at subcritical Reynolds numbers including reductions in recirculation and vortex formation length

*Contact author: a.ooi@unimelb.edu.au

along with stronger Reynolds stress. A similar effect has also been observed in the shear layer [10–13], where excitation at the shear layer frequency f_{SL} elicits a response in the power spectrum at f_{SL}, indicative of shear layer breakdown.

A similar, albeit more complex, scenario is the introduction of upstream turbulence, or free stream turbulence in the literature. Wake properties have been shown [14–17] to be drastically influenced by introduction of free-stream turbulence. These typically involve an accelerated transition to turbulence at subcritical Reynolds numbers, resulting in earlier formation of Kelvin-Helmholtz vortices within the shear layers. Moreover, vortex formation is moved upstream [18,19], leading to a shortened wake. However, this does not appear to majorly affect near wake spectral properties, with similar shedding frequencies reported by Lysenko [15] for turbulence intensities up to 10%. The effect on the shear layers on the other hand is more drastic. Khabbouchi *et al.* [19] found with increasing turbulence intensity, the subharmonic peak $f_{SL}/2$ became less energized, reflecting a suppression in pairing of Kelvin-Helmholtz vortices. Recent work by Kankanwadi and Buxton [17] also found an increase in the entrainment rate of background fluid into the wake and also enhanced wake meandering to freestream turbulence.

Recently, increased interest has been placed on research into confined bluff body flows due to their relevance in engineering applications, where nearby effects may influence the flow past the bluff body. For example, buildings are often located in cities, VIV energy converters have been found to be more efficient in channels [20,21], rotating cylinders placed close to the free surface as ship antirolling device [22], and wind turbines are located in farms. One such prototype flow that has been used to study confinement effects has been a cylinder placed centrally within a channel [23–33]. The additional length scale provided by the channel height introduces a second dimensionless parameter that describes the flow, the blockage ratio β, defined as the ratio of cylinder diameter to channel height. With varying blockage ratio and Reynolds number, a wide range of phenomena have been found by researchers. We refer the reader to the comprehensive review of Nguyen *et al.* [34]. However, we briefly recap some wake properties at $\mathrm{Re} = U_{\max}D/\nu = 3900$, which is considered presently. Ooi *et al.* [28] first considered this case for blockages of $\beta = 0.3$, 0.5, and 0.7. Their work found that wake properties were similar to the unconfined case for $\beta = 0.3$. Although, for $\beta = 0.5$, interactions between the shear layers separating from the cylinder, herein referred to as cylinder shear layers (CSLs), and wall shear layers (WSLs) result in changes to the wake topology and Reynolds stress distribution. Finally, for $\beta = 0.7$, shedding was suppressed and the mean wake was asymmetric. Further work by Lu *et al.* [29] found these wake asymmetries were modulated along the span. Different orientations of the asymmetric wake were observed along the spanwise direction with the wake flipping between the top and bottom walls. Despite the changes for each blockage, the CSLs were found to break down in all cases. Like with an unconfined flow, for cases with confinement, instabilities in the CSLs may be triggered by turbulence in the upstream [35], which in effect can alter development of the CSLs and subsequently, wake properties. Nguyen and Lei [36] considered a prototype flow of introducing harmonic disturbances upstream to a confined flow with blockage of $\beta = 0.6$. Four distinct lock-on regimes were observed. Within each regime, significant changes were found to the wake properties, with observed decreases in recirculation length and increases in fluctuating lift, which they determined were modulated by the CSLs. Hence, there exists a gap where one may consider "random" forcing as one might observe through introduction of turbulence upstream.

The objective of this work is therefore to investigate how upstream turbulence affects confined wake characteristics. Direct numerical simulations (DNSs) have been conducted with turbulence upstream of the cylinder, outlined in Sec. II. Comparisons are then made with the laminar upstream case of Ooi *et al.* [28] in Secs. III, IV, and V. Furthermore, focus is also placed in Sec. IV to understand how turbulence may affect formation of wake asymmetries in highly confined flows.

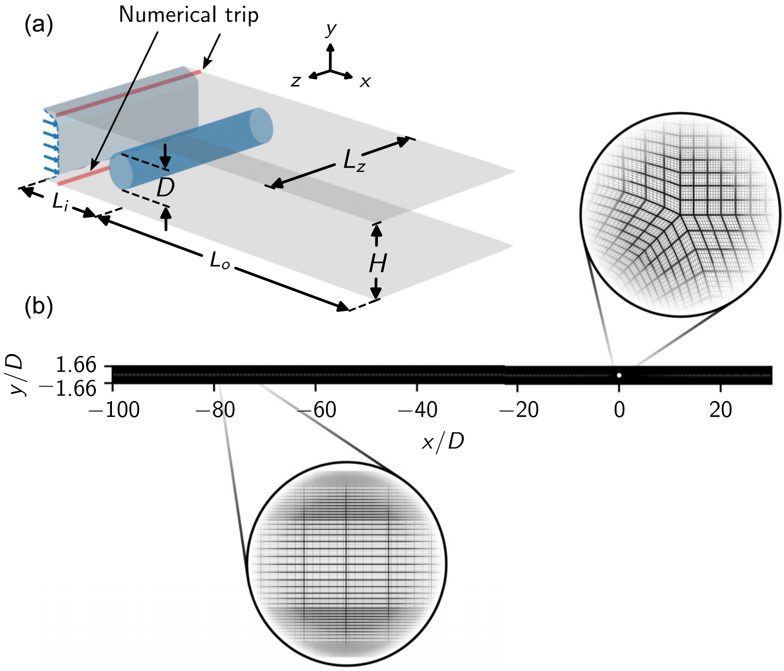

FIG. 1. Definition of problem considered in this study. (a) Schematic diagram of geometry and (b) mesh used for $\beta = 0.3$. Black (——) and gray (——) lines in (b) denote element boundaries of macro- and microelements, respectively.

II. PROBLEM FORMULATION

In this study, we consider a geometry consisting of a circular cylinder of diameter D that is placed centrally within a channel of height H as shown in Fig. 1(a). Streamwise, crossflow (normal to the channel walls), and spanwise directions are defined as x, y, and z, respectively.

Simulations were conducted using the spectral element code NekRS [37], which has been extensively used for bluff body [28,29], wall bounded [38,39], and density driven [40] flows. NekRS is a complete refactoring of Nek5000 [41], designed to target modern heterogeneous computing architectures [42]. Flow is simulated with the incompressible three-dimensional Navier-Stokes equations,

$$\nabla \cdot \boldsymbol{u} = 0, \tag{1a}$$

$$\frac{\partial \boldsymbol{u}}{\partial t} + \boldsymbol{u} \cdot \nabla \boldsymbol{u} = -\frac{1}{\rho} \nabla p + \nu \nabla^2 \boldsymbol{u}, \tag{1b}$$

where $\boldsymbol{u} = (u, v, w)$ are velocity components in the three orthogonal directions x, y, and z, p represents pressure, ρ density, and ν kinematic viscosity. There are two possible ways of defining the Reynolds number in such a flow based on whether one thinks of the geometry as a confined wake or a blocked channel flow. In the former case, we base the Reynolds number $\mathrm{Re}_D = U_b D/\nu$ on the bulk velocity U_b, cylinder diameter D, and kinematic viscosity ν. It is of note in the open literature, the centerline velocity upstream of the cylinder is also taken as a characteristic velocity scale [28]. However, this presents an issue when making comparisons with different upstream profiles. Hence, in this study, we consider the bulk velocity U_b to be most appropriate. If we now consider the latter description, then we instead define a channel Reynolds number as $\mathrm{Re}_b = 2U_b h/\nu$ with $h = H/2$

TABLE I. Mesh statistics for cases considered in the present study.

Case	L_z/D	E_{cyl}	E_{xy}	E_z	E_{elem}	N	Unique nodes
0p3	$5\pi/3$	40	15012	32	480384	7	165.27×10^6
0p5	π	32	8802	15	132030	9	96.65×10^6
0p7	π	40	6900	15	103500	9	75.85×10^6

being the half channel height, which is related to Re_D through

$$\mathrm{Re}_b = \frac{2U_b h}{\nu} = \frac{U_b H}{\nu} = \frac{U_b D}{\beta\nu} = \frac{\mathrm{Re}_D}{\beta}. \tag{2}$$

Within the turbulent regime Re_b naturally leads to another nondimensionalization based on inner scales of the flow. Such a scale is based on the wall shear stress $\tau_w = \mu d\overline{u}/dy|_w$, where μ is the dynamic viscosity, hence giving the friction velocity $u_\tau = \sqrt{\tau_w/\rho}$ as a characteristic velocity scale. Therefore, the friction Reynolds number is defined as

$$\mathrm{Re}_\tau = \frac{u_\tau h}{\nu}. \tag{3}$$

In this study, we first consider a Reynolds number of $\mathrm{Re}_D = 2600$ in order to match the bulk Reynolds number considered by Ooi *et al.* [28] so that direct comparisons can be made between the effect of fully laminar and turbulent upstream profiles.

For numerical discretization, Eq. (1) is cast into its weak form and approximated using the Galerkin method. The computational domain is then partitioned into E nonoverlapping elements within which the pressure and velocity fields are assumed to be represented by an Nth order polynomial basis defined at the Gauss-Lobatto-Legendre points. Statistics of each mesh are given in Table I and an example of the mesh used for $\beta = 0.3$ is shown in Fig. 1(b). Temporal advancement is provided using a third-order implicit/explicit method, where the diffusive terms are handled using a third-order backwards difference formula, and the convective terms using the operator-integrating-factor splitting scheme [43].

In our computational model, the inlet and outlet domains are also placed at a distance of $L_i/D = 100$ upstream (the long upstream domain is to ensure that the flow is fully developed when it interacts with the cylinder), and $L_o/D = 30$ downstream of the cylinder center. Finally, for the spanwise domain, we choose the maximum of $L_z/D = \pi$ and $L_z/h = \pi$. These values were chosen to match the work of Ooi *et al.* [28] and Zahtila *et al.* [44]. A visualization of the mesh is provided in Fig. 1(b) and an assessment of its quality is provided in Appendix A, satisfying the criterion set forth by Zahtila *et al.* [44] for statistical convergence. Although, may be considered slightly under-resolved following typical measures for DNS. Nevertheless, we are confident in the accuracy of the results presented.

For the boundary conditions, we apply no-slip conditions to the channel walls and cylinder surface. Periodicity is assumed along spanwise boundaries, and the stabilized outflow condition of Dong *et al.* [45] was applied to the outlet. Flow upstream was assumed to consist of a fully turbulent channel flow, the generation of which is discussed in the following section.

A. Turbulence generation

The technique of turbulence generation in numerical simulations is a nuanced issue. The simplest method of which, the recycling method [46], uses flow downstream of the inlet at some time t_n as a Dirichlet condition at time t_{n+1}. For unsteady flows, this results in strong temporal correlations in the flow, precluding reliable observation of temporal statistics [47]. To alleviate these issues, generation of a canonical turbulent channel flow is done through numerically tripping boundary layers of a laminar channel flow consisting of reflected Blasius boundary layers along both walls with 99%

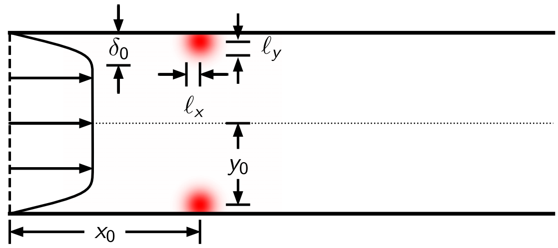

FIG. 2. Schematic diagram of the body force applied for flow tripping. Red contours represent the distribution of body force amplitude.

boundary layer thickness δ_0, which may be chosen arbitrarily, as we are interested in obtaining fully developed turbulent channel flow. Tripping was achieved using the method of Schlatter and Örlü [48] along the walls slightly downstream of the inlet, depicted in Fig. 2 and involves addition of a volumetric body force $\boldsymbol{F}$ to the Navier-Stokes equations

$$\frac{\partial \boldsymbol{u}}{\partial t} + \boldsymbol{u} \cdot \nabla \boldsymbol{u} = -\frac{1}{\rho} \nabla p + \nu \nabla^2 \boldsymbol{u} + \boldsymbol{F}. \tag{4}$$

This body force $\boldsymbol{F}$ is directed purely in the wall-normal direction, $\boldsymbol{F} = (0, F_y, 0)$, and has the form

$$F_y = \sum_{i=1}^{N_f} \underbrace{\exp\left[-\left(\left(x - x_0^{(i)}\right)/\ell_x\right)^2 - \left(\left(y - y_0^{(i)}\right)/\ell_y\right)^2\right]}_{\text{Spatial variation}} \underbrace{g(z,t),}_{\text{Temporal variation}} \tag{5}$$

where N_f is the number of points forcing is applied. The first term on the right-hand side localizes the body force about the point (x_0, y_0) along the streamwise-wall-normal plane with streamwise and wall-normal length scales of ℓ_x and ℓ_y, respectively. While $g(z,t)$ is a time-varying random forcing function given by

$$g(z,t) = A_t((1 - b(t))h^i(z) + b(t)h^{i+1}(z)), \tag{6}$$

where A_t denotes the amplitude of the volumetric force. The randomness in g here comes from randomly generating a unit amplitude harmonic signal every t_s time units, denoted by $h^i(z)$, where $i = \text{int}(t/t_s)$ is the number of time intervals that have passed in the simulation. Within these intervals, an interpolating polynomial $b(t) = 3p^2 - 2p^3$, with $p = t/t_s - i$ is used to continuously transition between $h^i(z)$ and $h^{i+1}(z)$. The spanwise variation of $h^k(z)$ has the form

$$h^k(z) = \sum_{n=0}^{N_m} a_n^k \sin\left(\frac{2\pi n z}{L_z}\right) + b_n^k \cos\left(\frac{2\pi n z}{L_z}\right), \tag{7}$$

where a_n^k and b_n^k are pseudorandom coefficients generated with unit amplitude $(a_n^k)^2 + (b_n^k)^2 = 1$.

B. Validation

To ensure the method described is capable of generating appropriate upstream conditions, we consider the development of turbulence in this section. To visualize this, we plot in Fig. 3 streamwise variation of friction Reynolds number Re_τ upstream of the cylinder. After an initial development region, Re_τ asymptotically approaches a constant value similar to that obtained using empirical correlations of Dean [49], represented by the dotted line and are also listed in Table II. It is of note that as we approach the cylinder, fluid accelerates through the gap, resulting in sharp increases

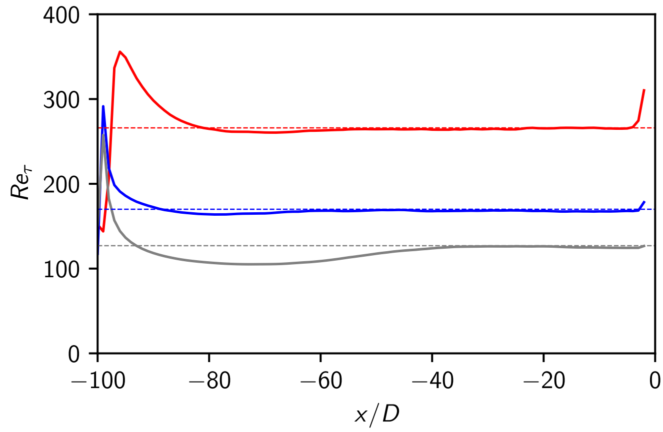

FIG. 3. Streamwise development of Re_τ for $\beta = 0.3$ (red line), $\beta = 0.5$ (blue line), and $\beta = 0.7$ (grey line). Dotted lines denote nominal Re_τ values computed using empirical correlations of Dean [49]. Note that the start of the cylinder is located at $x/D = -0.5$.

in wall stress and hence sharp spikes of Re_τ in Fig. 3. At low blockages, it appears the flow reaches a fully developed turbulent state relatively quickly, matching nominal values of Re_τ after $40D$ and $35D$ for $\beta = 0.3$ and 0.5, respectively. However, for $\beta = 0.7$, this development length is slightly longer at approximately $60D$. These variations are likely due to properties of the numerical trip rather than any physical mechanism. Most importantly though is that the flow reaches a fully developed state far upstream of the cylinder. Therefore to quantify the turbulent flow, we consider probing the flow at $x/D = -10$, values of Re_τ are given in Table II and show good agreement with the nominal values.

We next check whether the fully developed flow is representative of a canonical turbulent channel. Plotted in Fig. 4 are comparisons of first- and second-order turbulent statistics with results from simulations with a streamwise periodic channel at the same bulk Reynolds number. For time- and spanwise-averaged streamwise profiles, we find there is excellent agreement between the two datasets along with the log law. Moving onto turbulent statistics, both datasets again show excellent agreement. Hence, we are confident the presently used tripping method is capable of producing canonical turbulence upstream of the cylinder.

III. HYDRODYNAMIC COEFFICIENTS

To understand how turbulence upstream influences wake properties downstream, we begin by looking at its effects on hydrodynamic coefficients. We show in Table III differences in

TABLE II. Statistics of the turbulent upstream flow for each of the cases considered. Nominal Re_τ represents values obtained with empirical fits of Dean [49] and Re_τ computed values at $x/D = -10$.

Case	β	Re_b	Nominal Re_τ	Re_τ
0p3	0.3	8666.67	266.5	265.3
0p5	0.5	5200	170.5	167.4
0p7	0.7	3174.29	127.0	124.8

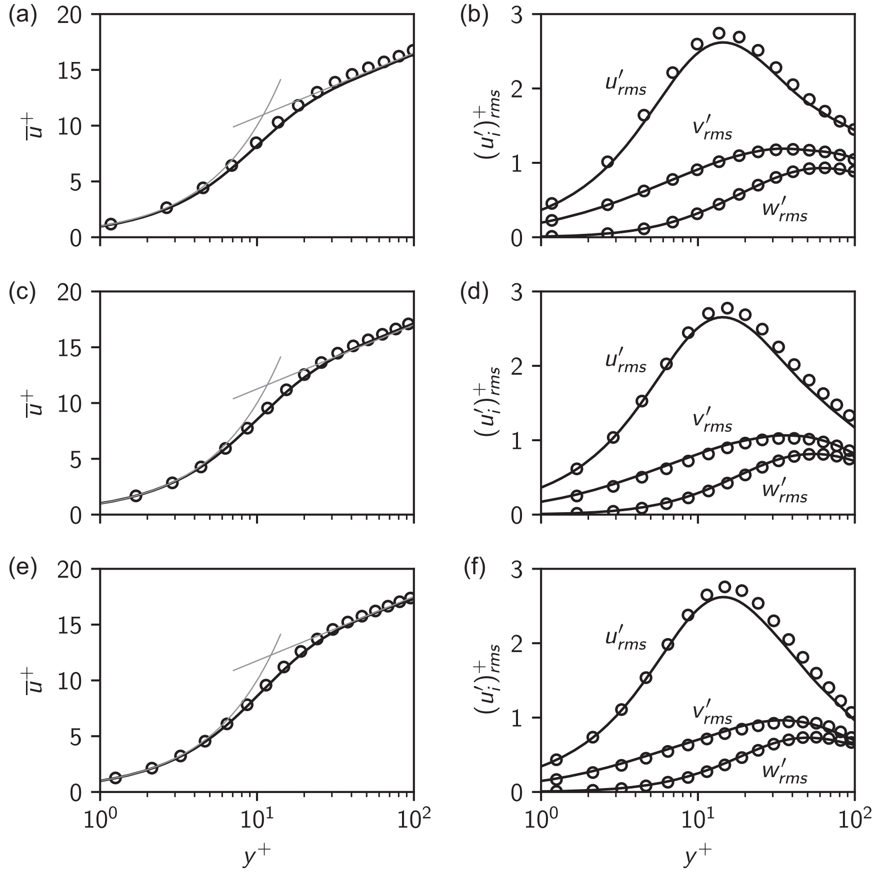

FIG. 4. Comparisons of time- and spanwise-averaged streamwise velocity profiles (left column) and turbulent statistics (right column) for [(a) and (b)] $\beta = 0.3$, [(c) and (d)] $\beta = 0.5$, and [(e) and (f)] $\beta = 0.7$. Comparisons are made between (——) present results, (——) log law, and (○) streamwise periodic results.

time-averaged drag $\overline{C}_D$ and fluctuating lift C'_L coefficients defined based on the bulk velocity

$$\overline{C}_D = \frac{\overline{F}_x}{\frac{1}{2}\rho U_b^2 D L_z}, \tag{8a}$$

$$C'_L = \frac{F'_y}{\frac{1}{2}\rho U_b^2 D L_z}, \tag{8b}$$

TABLE III. Comparison of hydrodynamic coefficients for cases with laminar and turbulent inflow conditions.

Upstream flow	β	$\overline{C}_D$	C'_L	$-C_{pb}$	St_b	L_r/D	L_v/D
Laminar	0.3	2.16	0.130	2.06	0.42	1.67	1.14
Turbulent		1.95	0.558	2.27	0.30	0.97	0.54
Laminar	0.5	3.50	0.096	4.05	0.72	1.46	1.04
Turbulent		3.34	0.315	4.27	0.51	1.42	1.38
Laminar	0.7	9.79	0.015	11.65		2.29	
Turbulent		9.84	0.059	13.20		2.70	

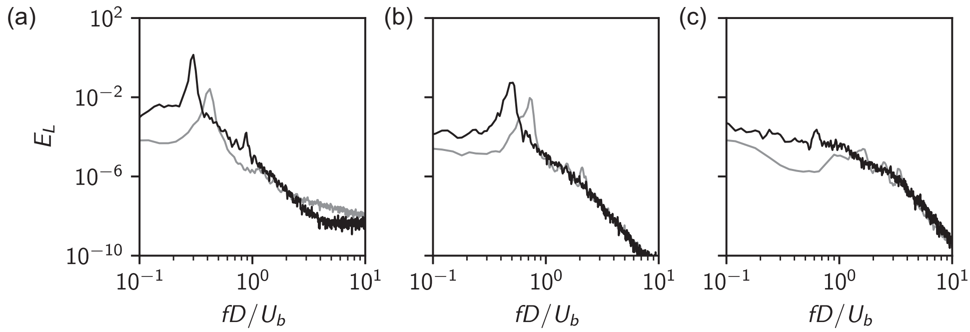

FIG. 5. Comparison of energy spectra generated from time-series of the lift coefficient E_L for (a) $\beta = 0.3$, (b) $\beta = 0.5$, and (c) $\beta = 0.7$ with laminar (——) and turbulent (——) upstream conditions.

where F_i denotes a force acting on the cylinder, with $\overline{F}_i$ and F_i' denoting time-averaged and root-mean-square, or fluctuating, forces, respectively. It is of note for all cases, the mean lift coefficient was observed to be zero including the asymmetric $\beta = 0.7$ case with laminar upstream conditions (LUCs) [28]. We find there is a slight decrease in time-averaged drag with the introduction of upstream turbulence for $\beta = 0.3$ and 0.5, while an increase occurs for $\beta = 0.7$. The result of $\beta = 0.3$ is surprising given drag increases are typical for unconfined bluff body flows where upstream turbulence is introduced [15,50]. Naturally, a direct comparison between upstream conditions is limited given that the time-averaged profiles are markedly different. Variations in upstream shear have been shown to produce different drag coefficients in confined flows [51]. Thus, it is likely these differences account for discrepancies with an unconfined cylinder. Although for fluctuating lift, a three to fourfold increase is observed for all β cases. Decomposition of $\overline{C}_D$ into pressure and viscous components found drag is dominated by its pressure component as is typical for bluff bodies [52]. Hence, we have also computed the base pressure coefficient C_{pb}, defined as

$$C_{pb} = \frac{p_b - p_\infty}{\frac{1}{2}\rho U_b^2}, \tag{9}$$

where p_∞ is taken as the centerline pressure at the inlet and p_b is the base pressure, that is, the pressure at the rear point of the cylinder wall. We find there is an increase in the magnitude of C_{pb}, similarly to that observed by Lysenko [15] in the unconfined case.

To interrogate timescales of the flow, we next consider the energy spectra of the lift coefficient in Fig. 5. We find for $\beta = 0.3$ and 0.5, clear peaks are observed in the spectra for both LUCs and turbulent upstream conditions (TUCs), corresponding to the frequency of the Kármán vortices formed and shed in the wake. We compute the Strouhal number based on U_b,

$$\mathrm{St}_b = \frac{f_p D}{U_b}, \tag{10}$$

where f_p is the frequency of this peak. A clear shift to frequencies approximately 35% lower occurs when switching from LUCs to TUCs. The reason behind this change is unclear at this point, but possible causes may include the interaction of turbulence with the CSLs or due to the change in upstream flow profile. At a higher blockage of $\beta = 0.7$, vortex shedding is suppressed as the wake becomes asymmetric [28], resulting in a much less notable peak at St ≈ 1.1, which Ooi *et al.* [28] attributed to merging of Kelvin-Helmholtz vortices formed in the CSLs. Meanwhile, with TUCs, the spectra lacks this peak, instead showing a decay in energy from low to high frequencies. Such an effect results from a recovery of wake symmetry, which will be discussed below.

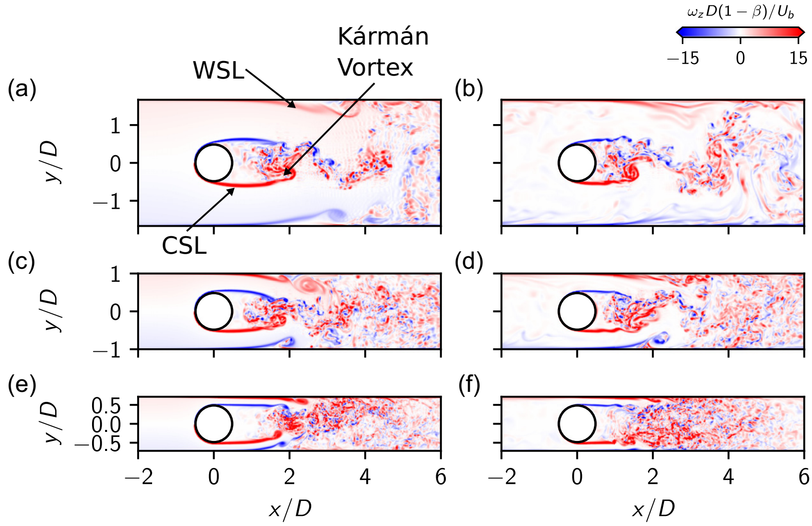

FIG. 6. Comparisons of instantaneous visualizations of spanwise vorticity normalized by gap velocity $\omega_z D(1-\beta)/U_b$ between a laminar inlet (left column) and a turbulent inlet (right column) for [(a) and (b)] $\beta = 0.3$, [(c) and (d)] $\beta = 0.5$, and [(e) and (f)] $\beta = 0.7$.

IV. FLOW TOPOLOGY

A. Instantaneous flow

To interrogate how changes in wake dynamics alter integral flow properties, we next consider instantaneous visualizations of spanwise vorticity ω_z. As wall shear and hence vorticity is maximized when fluid accelerates through gap, it is natural to normalized by the gap velocity scale U_g, which by continuity scales as

$$U_g \sim \frac{U_b}{1-\beta}. \tag{11}$$

Hence, in Fig. 6 contours of the quantity $\omega_z D/U_g = \omega_z D(1-\beta)/U_b$ are visualized. Note that the color scale appropriately captures flow structures for all blockage ratios, suggesting that U_g may be a more suitable velocity scale for this problem.

In the current and subsequent sections, comparisons are made between quantities of interest for laminar and turbulent upstream conditions. Data for flows with laminar conditions has been obtained from the the dataset of Ooi *et al.* [28]. For the smallest blockage of $\beta = 0.3$ in Figs. 6(a) and 6(b), we find for both cases vortex shedding is present. Such a result is expected as Khabbouchi *et al.* [19] was able to observe Kármán shedding in time traces when free-stream turbulence was introduced to an unconfined cylinder at a higher Reynolds number of $\mathrm{Re} = 4300$. The effect of turbulence was found to destabilize the CSLs further upstream. In this case, a laminar inlet shows laminar CSLs separating, with transition to turbulence occurring downstream at approximately $x/D = 1.5$ indicated by formation of Kelvin-Helmholtz vortices [28]. Meanwhile, with introduction of upstream turbulence, Kelvin-Helmholtz vortices form immediately after CSLs separate at $x/D \approx 0.5$, consistent with Khabbouchi *et al.* [19]. Once the CSLs destabilize, roll-up then occurs resulting in the formation of Kármán vortices. The earlier transition induced by upstream turbulence therefore leads to the earlier formation of Kármán vortices observed in Fig. 6(b). This also has the effect of inducing a crossflow flapping movement in the CSLs. The effect has also been observed in an unconfined cylinder [53], increases in Reynolds number in said case were instead responsible for a reduction of the vortex formation length. We demonstrate this effect in Fig. 7(b). The roll-up of the top CSL in Fig. 7(bi) pulls the CSL downwards. As the bottom layer begins to then roll-up [Fig. 7(bii)], a shift upwards

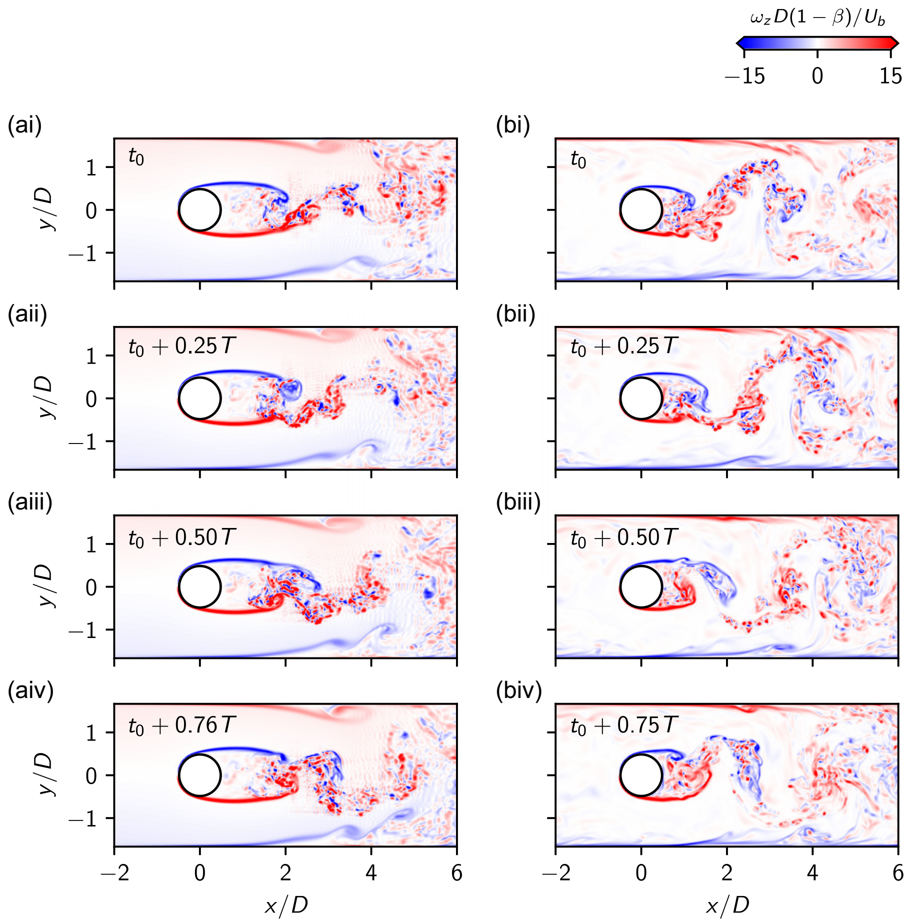

FIG. 7. Comparisons of instantaneous vorticity $\omega_z D(1-\beta)/U_b$ between (a) laminar and (b) turbulent upstream conditions over a single nondimensional period $T = 1/\mathrm{St}_K$ for a blockage of $\beta = 0.3$.

now occurs and at this point results in a balance where no deflection in the wake is observed. As further roll-up of the Kármán vortex occurs [Fig. 7(biii)], a shift upwards occurs where a similar effect occurs. This is unlike the case with LUCs, where the CSLs are extremely stable and roll-up occurs further downstream.

Somewhat similar observations may also be made for $\beta = 0.5$. Earlier break down of CSLs may again be observed and Kelvin-Helmholtz vortices are intensified, thus inducing larger pressure fluctuations near the cylinder. Hence, we find correspondingly larger fluctuations in the lift coefficient observed in Table III. However, the formation of Kármán vortices occurs at approximately the same location downstream between the two cases. We further interrogate the roll-up process in Fig. 8, where instantaneous realizations have been plotted over a single shedding period. Kármán vortex formation with LUCs is extremely similar to the $\beta = 0.3$ case with LUCs, we see the CSLs remain laminar and roll-up downstream of the cylinder. In contrast, with TUCs, CSL breakdown results in formation of Kelvin-Helmholtz vortices which are then entrained into the forming Kármán vortex. This is similar to the alternate shedding mode observed at $\beta = 0.6$ by Nguyen and Lei [27], where Kelvin-Helmholtz vortices form in the CSL before merging with Kármán vortices formed downstream. We also find there is minimal wake wandering in this case, possibly due to the roll-up location moving downstream or confinement effects limiting movement.

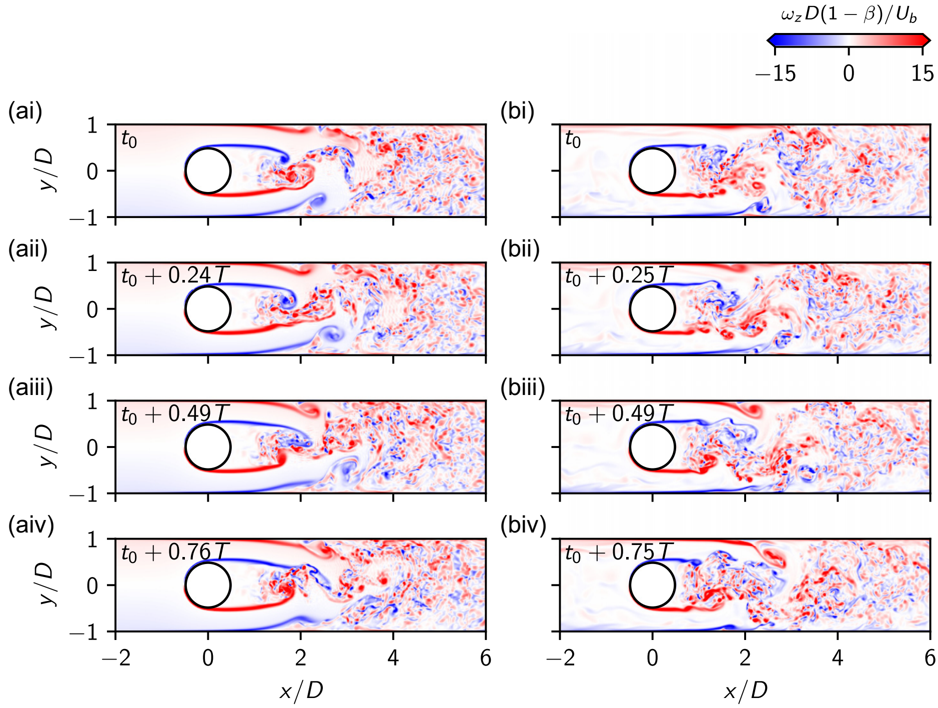

FIG. 8. Comparisons of instantaneous vorticity $\omega_z D(1-\beta)/U_b$ between (a) laminar and (b) turbulent upstream conditions over a single nondimensional period $T = 1/\mathrm{St}_K$ for a blockage of $\beta = 0.5$.

Finally, for the largest blockage of $\beta = 0.7$ in Figs. 6(e) and 6(f), it is known [28] for a laminar inlet wake bias occurs, which in this case is towards the top wall. A large recirculation region is formed along the bottom half of the domain once the bottom WSL separates. Both CSLs can be observed to merge downstream allowing for strong interactions between Kelvin-Helmholtz vortices and thus providing a small peak in the lift spectra [Fig. 5(c)]. With introduction of upstream turbulence, we find a significant alteration in wake topology for this case. The shear layers are again destabilized as soon as separation occurs, signified by small-scale Kelvin-Helmholtz vortices. Again, the earlier transition to turbulence induces larger fluctuations in pressure and wall stress, leading to larger values of C_L'. Unlike with LUCs, no wake bias is observed throughout the entire simulation (see Appendix B for details), with both CSLs remaining close to their respective walls. In absence of interaction between both CSLs, there is no longer a dominant timescale in the flow, leading to the gradual decay of energy observed in the lift spectra. As we progress further downstream, breakdown of the Kelvin-Helmholtz vortices occurs resulting in finer scale vortices being formed at approximately $x/D = 2$, which then begin to diffuse away from $x/D = 3$ indicating the flow begins to recover towards a canonical turbulent channel flow.

B. Time- and spanwise-averaged flow

Moving onto the time- and spanwise-averaged flow, visualizations of streamwise velocity are plotted in Fig. 9. Again, as fluid velocity is maximized through the gap, nondimensionalization is based on U_g. Large changes in wake topology may be observed with introduction of upstream turbulence. Beginning at the lowest blockage of $\beta = 0.3$, we find the wake is significantly shorter for TUCs as indicated by changes in contours of $\overline{u} = 0$. We also find with upstream turbulence, recirculation bubbles along both walls are significantly smaller, with reattachment occurring significantly further upstream making it difficult to observe in Fig. 9(b). Hence, streamwise velocity is more

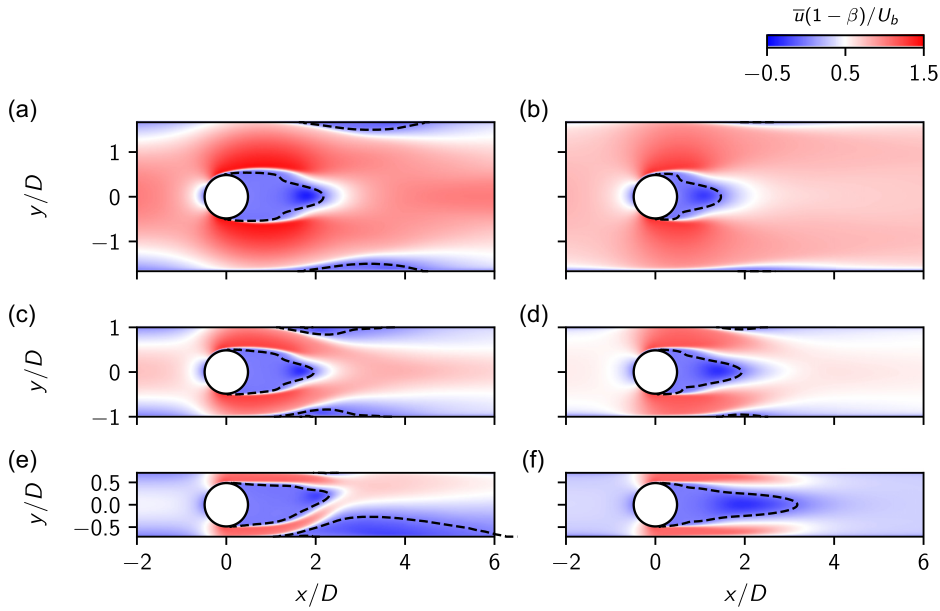

FIG. 9. Comparisons of time- and spanwise-averaged streamwise velocity normalized by gap height $\overline{u}(1-\beta)/U_b$ between a laminar inlet (left column) and a turbulent inlet (right column) for [(a) and (b)] $\beta = 0.3$, [(c) and (d)] $\beta = 0.5$, and [(e) and (f)] $\beta = 0.7$. Overlain are contours of $\overline{u}(1-\beta)/U_b = 0$ (- - - -).

evenly distributed across the channel downstream of the cylinder, which suggests an accelerated recovery to a turbulent channel flow. Such a topic may be of interest to future researchers, but is out of scope for this study. With increasing blockage at $\beta = 0.5$, both wakes appear to be of comparable size, although downstream, for $x/D > 2$, accelerated flow recovery occurs with TUCs, as may be observed by comparatively lower velocities along the channel core and higher velocities near the walls. Again, we find recirculation bubbles along the channel walls are smaller. To understand this further, we plot in Fig. 10 time- and spanwise-averaged velocity profiles downstream of the gap. For $\beta = 0.3$ and 0.5, near the gap, velocity profiles are skewed more towards the wall with TUCs compared with LUCs. Upstream turbulent structures induce strong mixing which transfers momentum from the outer regions towards the wall. Hence, this increased momentum near the wall enables for the boundary layer to remain attached for longer and accelerates reattachment when it does separate.

Finally, for $\beta = 0.7$, a laminar upstream has previously been shown [28] to result in wake asymmetries. However, surprisingly the introduction of upstream turbulence reintroduces symmetry to the solution. Lu *et al.* [29] found that symmetry may be recovered in time- and spanwise-averaged flow fields for such a flow configuration due to spanwise modulated wake asymmetries. Observations of the instantaneous flow at various times show no modulation along the span (Appendix B). Another possibility may be the occurrence of bistabilities in flow. For example, flow past side-by-side cylinders is known to demonstrate intermittent switching between two asymmetric states, which has been hypothesized to be caused by interactions with gap vortices [54]. Similarly, bistable behavior has also been observed in Ahmed bodies [55–57], where switches between both states have been proposed to occur due to hairpin vortices shed from the body [58]. As observed in the prior section, the wake demonstrates no bias, meaning that wake jumping no longer occurs. Thus, bistability is unlikely to be the cause of symmetry recovery. Rather, we pose that global symmetry is a result of upstream turbulence disrupting formation of large-scale wake structures, which we explore in a subsequent section.

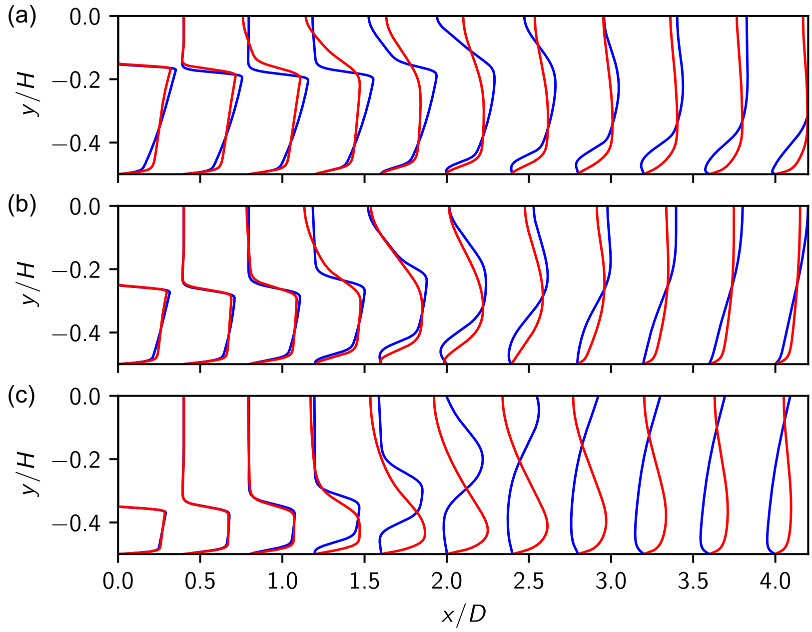

FIG. 10. Comparisons of flow profiles for laminar (——) and turbulent (——) upstream conditions at blockage ratios of (a) $\beta = 0.3$, (b) $\beta = 0.5$, and (c) $\beta = 0.7$.

To quantify observations of wake length changes, we plot in Fig. 11 time- and spanwise-averaged streamwise velocity along the centerline $y/D = 0$ for each blockage ratio. As focus is placed on flow downstream of the cylinder, nondimensionalization is instead done with U_b. As previously done, the wake length, L_r, is defined as the furthest point downstream along the $\overline{u} = 0$ contour. For globally symmetric flows, this point occurs along the centerline, $y/D = 0$, which is demarcated in Fig. 11 by open and solid circles for laminar and turbulent inflows, respectively. Values of L_r/D are given in Table III. Note that for $\beta = 0.7$, as LUCs result in wake asymmetries, the centerline velocity is an inappropriate measure of wake length. Hence, no marker is plotted for said case. We find there appears to be a general increase in wake length with blockage for a turbulent inlet. However, it is surprising though that while the recirculation length is shorter for a turbulent inflow compared with a laminar one at $\beta = 0.3$, both are of comparable length at $\beta = 0.5$, and for $\beta = 0.7$, observation of the $\overline{u}/U_b = 0$ contour in Figs. 9(e) and 9(f) finds the turbulent case is visually longer. Effects of free-stream turbulence have previously been suggested to lead to shorter observed wakes in an unconfined cylinder [59,60] and are likely responsible for $\beta = 0.3$ here as well. We also find that $U_{\min}$, the most negative value of $\overline{u}$ also appears to be larger in magnitude for laminar compared with turbulent upstream flows. Parnaudeau *et al.* [60] also observed variations in $U_{\min}$ for an unconfined cylinder and suggested that it may be sensitive to a mixture of aspect ratio and blockage. Our present results here indicate that upstream turbulence may also further contribute to these uncertainties. Meanwhile, for $\beta = 0.5$, despite similarities in L_r, profiles of $\overline{u}$ are remarkably different. Both cases decrease before showing a gradual increase to an asymptotic value of $\overline{u}/U_b \approx 1.1$. However, within the recirculation bubble, we find the dip occurs closer to the cylinder for TUCs compared with LUCs. It appears increased destabilization in the CSLs induces more energetic structures close to the cylinder [Fig. 6(d)], leading to this change. Further downstream, a laminar inflow results in a steep recovery with a distinct bump near $x/D = 3$, which is much reduced for TUCs. Finally, for $\beta = 0.7$, profiles are distinctly different due wake asymmetries being observed for LUCs. For a turbulent inflow though, much like the other blockages, the dip occurs immediately downstream of

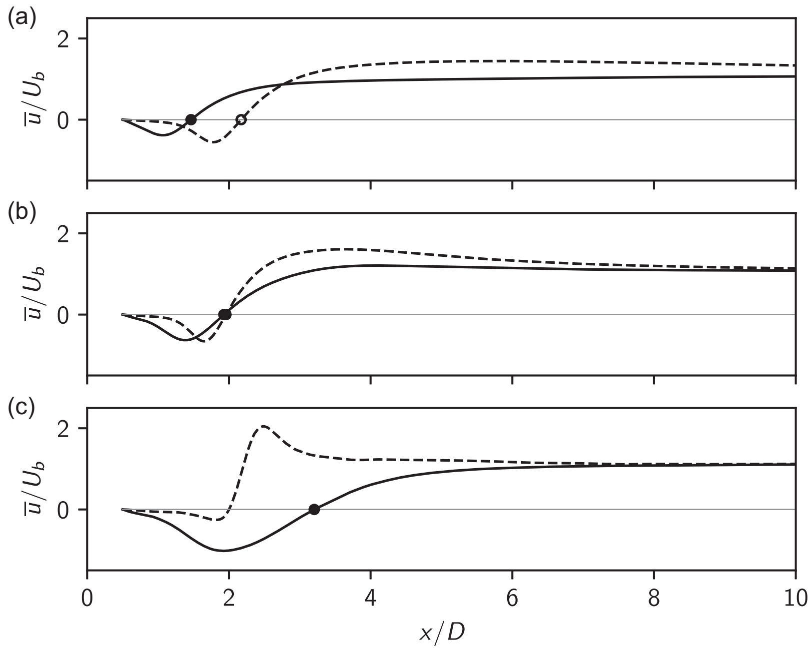

FIG. 11. Time- and spanwise-averaged streamwise velocity $\overline{u}/U_b$ along the centerline $y/D = 0$ for laminar (- - - -) and turbulent (——) upstream conditions with recirculation lengths demarcated by (○) and (•), respectively. Comparisons have been made for blockages of (a) $\beta = 0.3$, (b) $\beta = 0.5$, and (c) $\beta = 0.7$.

the cylinder, which is again a result of turbulent structures being formed within the recirculation region.

C. Turbulent statistics

In previous sections, the presence of turbulence upstream was qualitatively found to induce earlier transition in both CSLs and WSLs. To quantify and compare this between the two cases, we interrogate turbulent statistics in this section. Visualizations of the streamwise fluctuations $\overline{u'u'}/U_b^2$ are given in Fig. 12. Immediately, we find that as blockage increases, fluctuations in u increase as well. It is of note that nondimensionalization by U_g, not depicted here, reversed the trend with $\beta = 0.3$ showing large levels of fluctuations and $\beta = 0.7$ showing low levels. The effect is due to the highest fluctuation features being downstream of the CSLs. Hence, nondimensionalization by U_g is not applicable for Reynolds stresses.

Looking at the effects of upstream turbulence, strong modification to the Reynolds stresses are found, reflecting changes observed in prior sections. For $\beta = 0.3$, the shape of $\overline{u'u'}$ is significantly different between both cases. For LUCs, two peaks occur at the ends of the CSLs at approximately $x/D = 1.8$ appearing due to formation of Kármán vortices and their eventual convection downstream. However, with TUCs, $\overline{u'u'}$ is evenly spread in the CSLs and is of comparable magnitude to the values at the ends. This increase in Reynolds stresses in the CSLs results from earlier breakdown induced by turbulent structures passing through the gap tripping the shear layers. Comparison with contours of $\overline{u'u'}$ computed by Song *et al.* [50] for an unconfined cylinder under TUCs and LUCs finds strong similarities in the structure of the Reynolds stresses. However, given the low blockage, such results are expected given the weak interaction between CSLs and WSLs. Increasing blockage to $\beta = 0.5$, Reynolds stresses for LUCs display a similar structure to $\beta = 0.3$, consisting of two peak at the ends of the CSLs. However, there is now an additional contribution due to separation and breakdown of WSLs. Comparing with the TUC case, the structure is similar between both

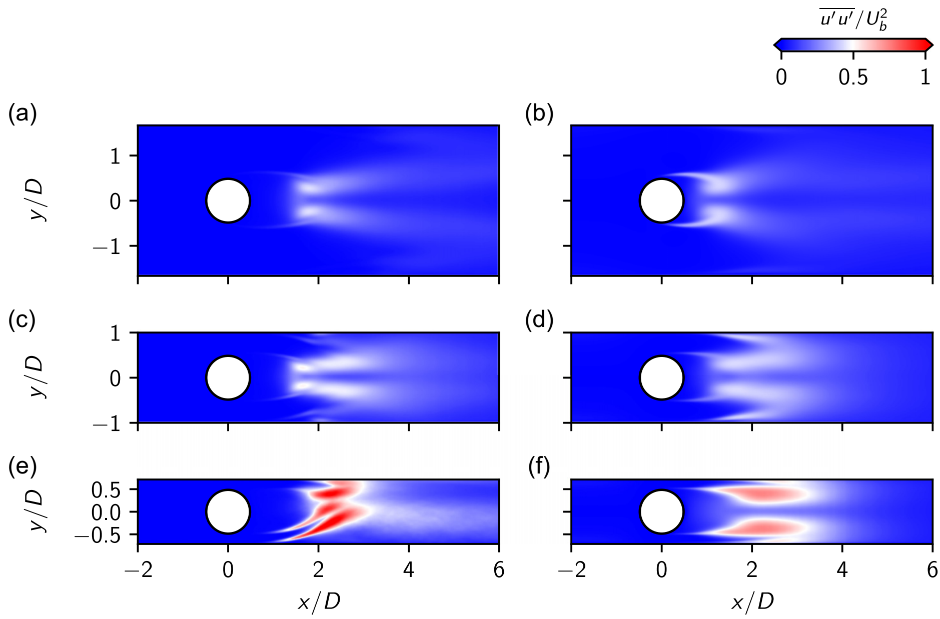

FIG. 12. Comparisons of streamwise normal Reynolds stress $\overline{u'u'}/U_b^2$ between a laminar inflow (left column) and a turbulent inflow (right column) for [(a) and (b)] $\beta = 0.3$, [(c) and (d)] $\beta = 0.5$, and [(e) and (f)] $\beta = 0.7$.

cases with some subtle differences reflecting changes in wake dynamics. Like with $\beta = 0.3$, there is more energy in the CSLs near the cylinder due to break down via interaction with turbulent structures convected through the gap. However, these levels of fluctuations are lower than $\beta = 0.3$. A similar trend is also observed for $\beta = 0.7$. This effect is caused by relaminarization of the flow as it accelerates through the gap [61], which has been quantified with profiles of $\overline{u'u'}/U_b^2$ from upstream to downstream of the cylinder in Fig. 13. Note the same scale for $\overline{u'u'}/U_b^2$ in Figs. 13(a) and 13(b). Moving from a point upstream of the cylinder to the its center, $\overline{u'u'}$ decreases near the walls and increases along the cylinder due to the formation and subsequent separation of the CSL. The effects are most notable for $\beta = 0.5$ and 0.7, where streamwise acceleration is strongest, while for $\beta = 0.3$

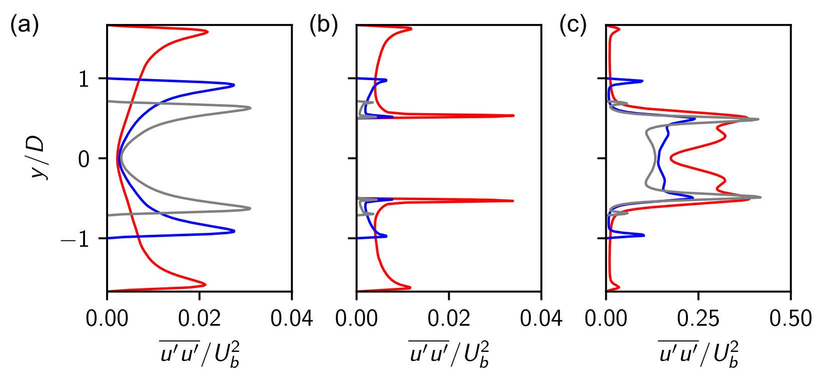

FIG. 13. Profiles of streamwise normal Reynolds stress $\overline{u'u'}/U_b^2$ with turbulent upstream conditions for $\beta = 0.3$ (red line), $\beta = 0.5$ (blue line), and $\beta = 0.7$ (gray line) at streamwise locations of (a) $x/D = -1$, (b) $x/D = 0$, and (c) $x/D = 1$.

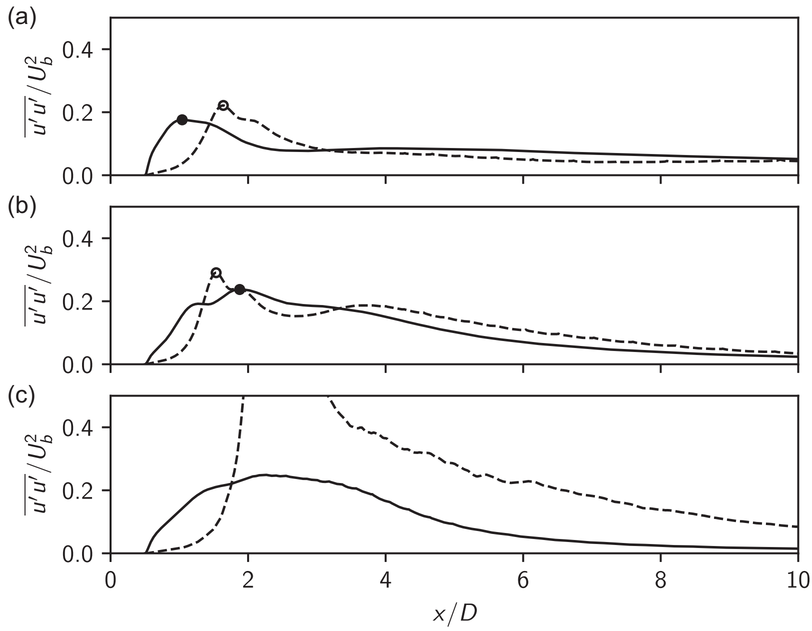

FIG. 14. Profiles of streamwise normal Reynolds stress $\overline{u'u'}/U_b^2$ along the centerline $y/D = 0$ for laminar (- - - -) and turbulent (——) upstream conditions with vortex formation lengths demarcated by (○) and (●), respectively. Comparisons have been made for blockages of (a) $\beta = 0.3$, (b) $\beta = 0.5$, and (c) $\beta = 0.7$.

it is somewhat minimal due to acceleration occurring predominantly occurring near the cylinder rather than the channel walls. Further downstream at $x/D = 1$, for all cases, $\overline{u'u'}$ has increased in magnitude from shear layer break down. Also considered is the streamwise development of $\overline{u'u'}/U_b^2$ along the centerline, $y/D = 0$, in Fig. 14. For $\beta = 0.3$, the profile peak occurs further upstream for TUCs compared with LUCs. Such a point denotes the vortex formation length L_v, which has been computed in Table III and marks the point where Kármán vortices begin to form. For an unconfined flow, Khabbouchi *et al.* [19] found the tripping effect free-stream turbulence has on shear layers effectively moves this point upstream, resulting in a shortened wake, which also appears to be the case for $\beta = 0.3$. However, for $\beta = 0.5$, both points are relatively similar. It is possible relaminarization of the flow through the gap, while still inducing transition upstream, is not strong enough for shift L_v. This seems to be well correlated with findings made by Khabbouchi *et al.* [19], who determined a monotonic decrease in L_v with increasing free-stream turbulence intensity. However, it would be remiss to not mention the lower friction Reynolds number as blockage increases also playing part into this.

Looking at flow downstream for $\beta = 0.7$, for LUCs, strong fluctuations occur in the CSLs along with the WSLs due to their separation and break down. However, with TUCs, only the CSLs experience strong fluctuations due to the formation of Kelvin-Helmholtz vortices. As no separation is observed in the WSLs, only low levels of $\overline{u'u'}$ occur at the channel walls. Similarly to low blockages, TUCs result in earlier breakdown and hence larger streamwise normal Reynolds stresses close to the cylinder, which are of a comparable level to the other cases [Fig. 13(c)].

Moving to the crossflow normal Reynolds stresses, Fig. 15 depict contours of the quantity $\overline{v'v'}/U_b^2$. For blockages of $\beta \leqslant 0.5$, there is an intense region of fluctuations downstream at approximately $x/D = 2$ corresponding to Kármán vortices inducing strong crossflow motions before diffusing out as interactions with WSLs cause break down into smaller scale structures. Comparing between different inflow conditions, both profiles are found to be extremely similar at $\beta = 0.3$, while for $\beta = 0.5$ the peak is much stronger with LUCs. For the largest blockage $\beta = 0.7$, it can be

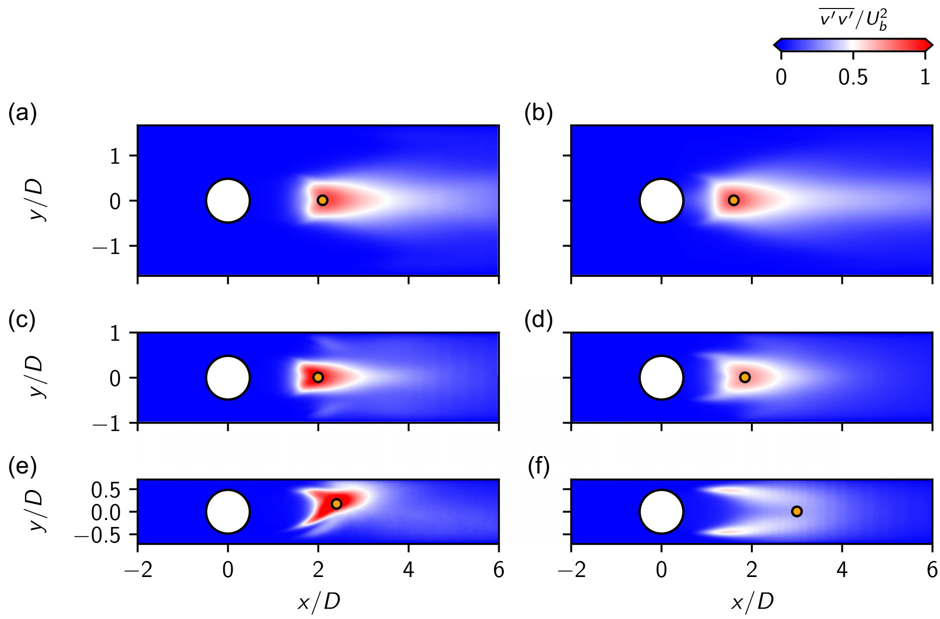

FIG. 15. Comparisons of crossflow normal Reynolds stress $\overline{v'v'}/U_b^2$ between a laminar inlet (left column) and a turbulent inlet (right column) for [(a) and (b)] $\beta = 0.3$, [(c) and (d)] $\beta = 0.5$, and [(e) and (f)] $\beta = 0.7$. Orange dots demarcate points where spectra are computed in Fig. 18.

seen for LUCs [Fig. 15(e)] interactions between turbulent structures formed in both CSLs result in a large peak downstream, which is skewed towards the top wall by wake asymmetries. Meanwhile, for TUCs, the tendency for both CSLs to stick near their respective wall reduces the intensity of crossflow fluctuations and localizes the peak to within the CSLs. As the Kelvin-Helmholtz vortices formed within each CSL break down into finer scale structures, $\overline{v'v'}$ gradually diffuses out downstream to reflect this.

D. Recovery of wake symmetry

The prior sections demonstrate the presence of global symmetry recovery at $\beta = 0.7$ with the introduction of upstream turbulence. Hence, in this section, we investigate possible mechanisms involved in this process. The general hypothesis [28,29] behind wake asymmetries rests in the coupling between the WSL and CSL. This effect may be visualized through the concurrent formation of vortices in Figs. 6(a), 6(c), and 6(e) with increasing blockage. Based on this interpretation, if we interrupt the coupling, then a recovery of symmetry may occur. Through imposition of slip boundaries along the channel walls, Lu *et al.* [32] were able to separate the effect of confinement and wall-wake interactions. The elimination of the WSLs at high blockage ratios, removing the latter effect, was found to result in symmetry recovery.

In the present case, the observation in the prior sections of increased Reynolds stresses near the cylinder [Fig. 12(f)] found earlier break down in the CSLs once turbulence is introduced upstream. We therefore postulate that the early breakdown caused by upstream turbulent structures decouples the CSLs and WSLs. Therefore, inhibiting the formation of flow asymmetry.

To test this, we now investigate the coupling between WSL and CSL. As a measure of the flow, time series of velocity have been computed in both the WSL and CSL, as shown in Figs. 16(a) and 17(a). The coupling between the two shear layers may then be measured through computation of a correlation coefficient R. Such techniques have previously been used to quantify interactions between large- and small-scale structures in a turbulent boundary layer [62,63]. We therefore

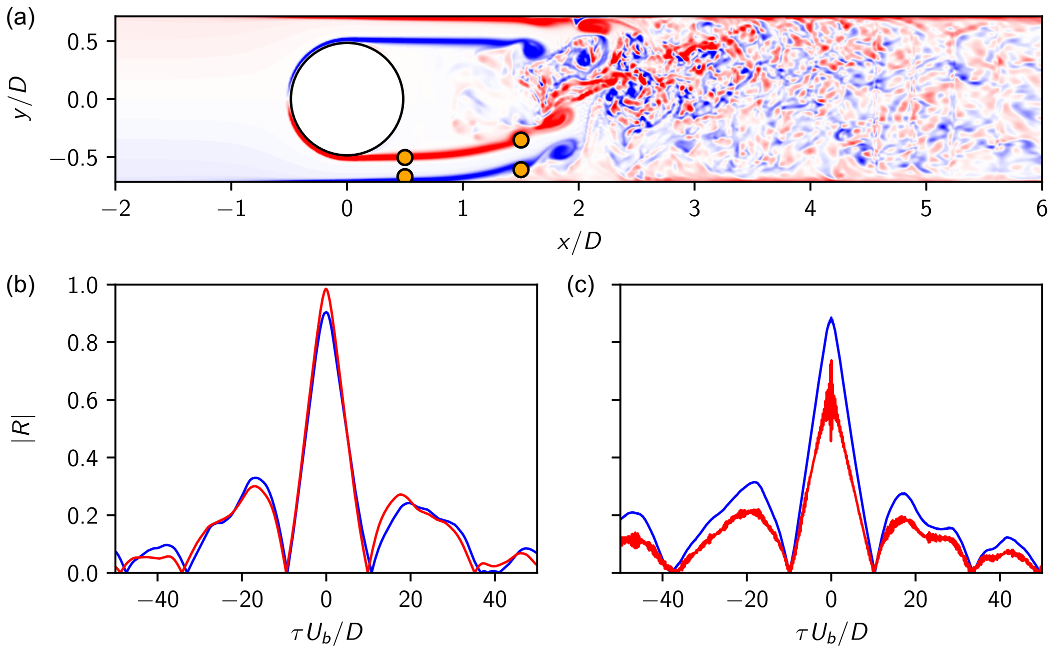

FIG. 16. Variation in coupling between cylinder shear layers and wake shear layers for $\beta = 0.7$ with laminar upstream conditions. (a) Visualization of probe locations (orange dots) and cross-correlation functions, $|R|$, for streamwise (blue) and crossflow (red) velocities at streamwise locations of (b) $x/D = 0.5$ and (c) $x/D = 1.5$.

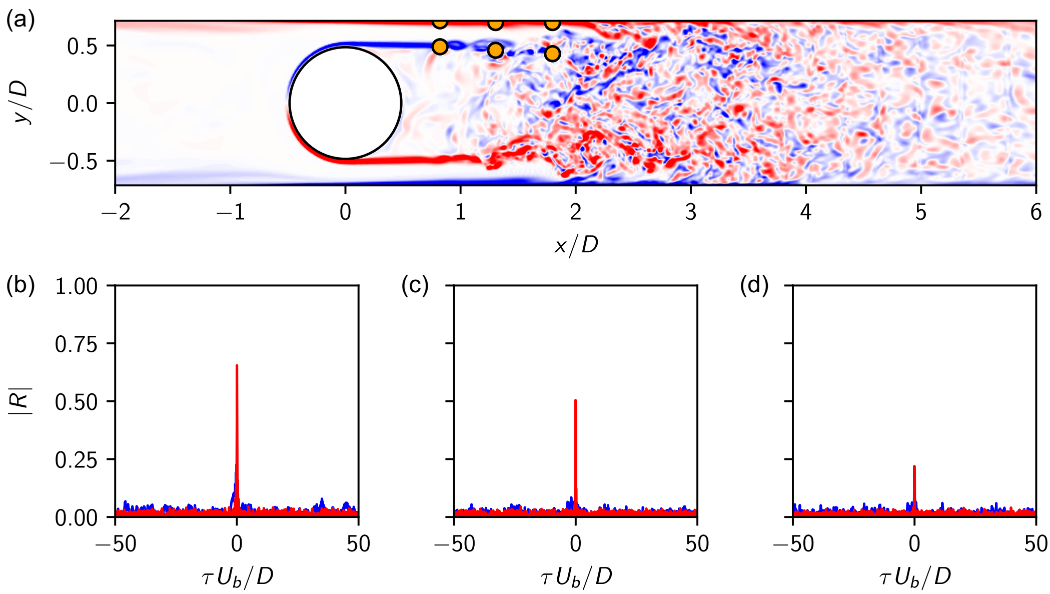

FIG. 17. Variation in coupling between cylinder shear layers and wake shear layers for $\beta = 0.7$ with turbulent upstream conditions. (a) Visualization of probe locations (orange dots) and cross-correlation functions, $|R|$, for streamwise (blue) and crossflow (red) velocities at streamwise locations of (b) $x/D = 0.82$, (c) $x/D = 1.3$, and (d) $x/D = 1.8$.

define a cross-correlation function between the two time series u_i^W and u_i^C, for the WSL and CSL, respectively, as

$$R\left(u_i^C, u_i^W; \tau\right) = \overline{\tilde{u}_i^C(t+\tau)\tilde{u}_i^W(t)}, \tag{12}$$

where $\tilde{u}$ denotes a time series, u, normalized to have mean zero and unit variance and τ denotes the time lag. To quantify the coupling with both LUCs and TUCs, we compute the cross-correlation R of both streamwise, u, and crossflow, v, velocities at various streamwise locations within the respective shear layers. These probes are placed both before and after the point of turbulent transition, depicted in Figs. 16(a) and 17(a) along with plots of the absolute value of the cross-correlation function, $|R|$. As u is normalized to have unit variance, then $|R|$ is bounded above by unity, providing a method to quantify the strength of the coupling.

Beginning with LUCs, we plot $|R|$ in Figs. 16(b) and 16(c) before and after the formation of Kelvin-Helmholtz vortices, respectively. At both streamwise locations, $|R|$ is maximized for $\tau \approx 0$, with values of at least 0.8 for both streamwise and crossflow velocities. Hence, indicating a strong coupling between both CSLs and WSLs pre- and post-transition, consistent with observations made in the prior section. Meanwhile, for TUCs, Figs. 17(b)–17(d) shows that as we progress in the streamwise direction, the maxima of $|R|$ decreases from a value of approximately 0.7 at $x/D = 0.82$ to 0.5 at $x/D = 1.3$ and, finally, 0.2 at $x/D = 1.8$, showing the two signals decorrelate as we move downstream. As the three points mark the CSL being laminar, forming Kelvin-Helmholtz vortices, and finally being turbulent [Fig. 17(a)], then it is possible to interpret this as evidence of the WSL and CSL decoupling with breakdown of the CSL. Since, the incipience of CSL breakdown is caused by upstream turbulence tripping the shear layer, it is likely the process of symmetry recovery occurs due to the mechanism responsible for wake asymmetry being unable to enact on the flow. This also suggests that whatever this mechanism is, it is localized to the rear of the wake and its action may be broken by decoupling the WSL and CSL, which is consistent with findings made by Lu *et al.* [32].

As the transition point is known to move upstream with Reynolds number [7], shear layer decoupling may also occur with increases in Reynolds number, thus leading to symmetry recovery at sufficiently large Reynolds numbers irrespective of upstream conditions. This also implies that observations of wake asymmetry are limited to sufficiently low Reynolds numbers. Hence, future extensions to this work may involve studying the Reynolds number effect on symmetry recovery. However, testing of this hypothesis is out of scope for the present study and will be left to future work.

V. SPECTRAL ANALYSIS

In previous sections, vortex shedding was observed in the wake for blockage ratios of $\beta = 0.3$ and 0.5 with LUCs and TUCs. Although, for $\beta = 0.7$, shedding was found to be suppressed for both sets of inflow conditions. The CSLs were also found to break down into Kelvin-Helmholtz vortices for both cases. Investigation into timescales of the flow was also conducted through analysis of C_L; however, it is limited by C_L being based on surface quantities along the cylinder. Hence, in this section, we further investigate the timescales of the flow with placement of probes at different points of the wake.

A. Wake properties

Beginning with analysis of vortex shedding, we place probes along the regions of maximal $\overline{v'v'}/U_b^2$, chosen due to shed Kármán vortices inducing large crossflow velocity fluctuations when convected pass the probe location. The points lie on the centerline $y/D = 0$ for $\beta = 0.3$ and 0.5 as the time- and spanwise-averaged flow is symmetric, as demarcated by the orange dots in Figs. 15(a)–15(d). However, for $\beta = 0.7$, the flow asymmetry with LUCs requires placement of a

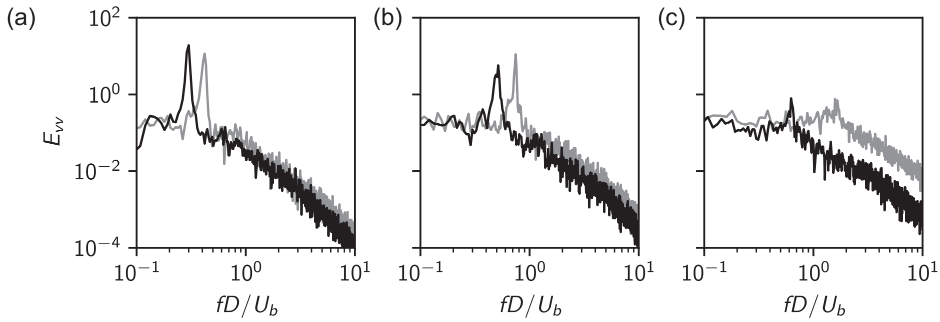

FIG. 18. Comparison of energy spectra generated from time series of crossflow velocity v/U_b for (a) $\beta = 0.3$, (b) $\beta = 0.5$, and (c) $\beta = 0.7$ with laminar (——) and turbulent (——) upstream conditions.

probe off center, at the point $(x/D, y/D) = (2.4, 0.17)$ [Fig. 15(e)]. Although, with TUCs, maxima of $\overline{v'v'}/U_b^2$ lie within the CSLs, which we will consider in the subsequent section. Hence, for consistency, the probe has been placed at the maximal value on the centerline $(x/D, y/D) = (3, 0)$ [Fig. 15(f)] . Beginning with $\beta = 0.3$ and 0.5, Figs. 18(a) and 18(b) shows distinct peaks at St_b, coinciding with peaks of the lift spectra in Figs. 5(a) and 5(b). This is due to the onset of Kármán shedding being a global instability, where the instability mode extends over the entire domain [64]. We also find for $\beta = 0.5$ [Fig. 18(b)], the higher frequency components with TUCs contain less energy than those with LUCs, which explains the smaller values of $\overline{v'v'}$ with TUCs in Figs. 15(c) and 15(d). Moving onto $\beta = 0.7$, Fig. 18(c) shows that for LUCs, a peak occurs at approximately $fD/U_b = 1.65$, which Ooi *et al.* [28] hypothesized was caused by vortex pairing from Kelvin-Helmholtz vortices from the CSLs. However, with TUCs, we find that a peak occurs at $fD/U_b \approx 0.65$. The appearance of this peak is surprising, especially since no vortex shedding may be observed in the flow.

B. Instabilities in the cylinder shear layers

We now turn our focus to timescales of instabilities in the CSLs, and begin with the lowest blockage case of $\beta = 0.3$. A number of probes have been placed along the spanwise plane $z/D = 5\pi/6$, which has been arbitrarily chosen due to the flow being homogeneous in the span. Within the plane, choice of probe locations is based on where Kelvin-Helmholtz vortices were observed to form, which in wake flows typically occurs where $\overline{u'u'}/U_b^2$ is maximal. However, due to the wandering of the CSLs previously observed, these regions do not always coincide. Hence, we have chosen probe locations of $(x/D, y/D) = (0.28, \pm 0.59)$, $(0.52, \pm 0.64)$, and $(0.80, \pm 0.65)$, demarcated by the orange dots in Figs. 19(b) and 19(c). We see in the instantaneous flow [Fig. 19(b)] the probes on the top half of the domain lie within the CSL, while those on the bottom are slightly below the CSL. As a result, the probes do not lie within the regions of maximal Reynolds stress intensity. In Fig. 19(a), we plot energy spectra of streamwise velocity at these points, which has been averaged between top and bottom probes due to the crossflow symmetry of the flow. For all probe locations, two prominent peaks occur at the vortex shedding frequency $\mathrm{St}_K = 0.29$ and its first harmonic 0.58. The presence of these peaks again results from vortex shedding being a global instability but may be interpreted physically as the wandering frequency of the CSLs. At higher frequencies, the probe closest to the cylinder $(x/D, y/D) = (0.28, \pm 0.59)$ shows a bump at approximately $fD/U_b = 2$. With increasing streamwise position, this develops into a small peak at $(x/D, y/D) = (0.52, \pm 0.64)$, with frequency $\mathrm{St}_{\mathrm{SL}} \approx 1.95$, which we interpret as the shear layer frequency. For the furthest probe from the cylinder $(x/D, y/D) = (0.80, \pm 0.65)$, the spectrum shows a sharp change from a constant spectral amplitude to decay at the shear layer frequency. This is unlike the case with LUCs, where Ooi *et al.* [28] found a distinct peak at $\mathrm{St}_{\mathrm{SL}} \approx 2.5$ (1.67 in terms of their scaling using the upstream

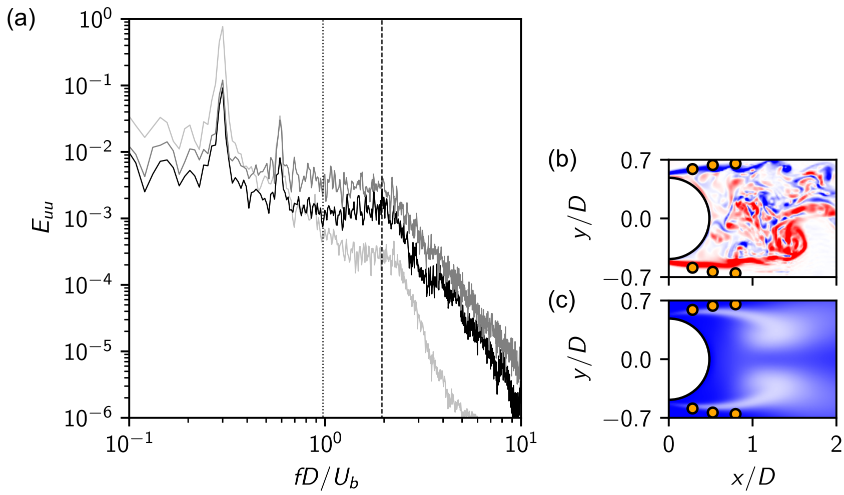

FIG. 19. Energy spectra (a) of streamwise velocity at $(x/D, y/D) = (0.28, \pm 0.59)$ (——), $(x/D, y/D) = (0.52, \pm 0.64)$ (——), and $(x/D, y/D) = (0.80, \pm 0.65)$ (——) for $\beta = 0.3$. Dashed (- - - -) and dotted (.......) lines denote $\mathrm{St_{SL}}$ and $\mathrm{St_{SL}}/2$, respectively. Visualization of probe locations in (b) instantaneous spanwise vorticity $\omega_z D/U_b$ and (c) streamwise normal Reynolds stress $\overline{u'u'}/U_b^2$ fields.

centerline velocity). Subsequent comparisons with Ooi *et al.* [28] will also denote frequencies scaled in terms of centerline velocity with brackets. The unenergetic peak is typical for spectra of velocity signals within CSLs. Intermittent appearance of Kelvin-Helmholtz vortices result in energy bleeding to surrounding frequencies [65,66]. In the present case, this is further exacerbated by wake wandering, resulting in Kelvin-Helmholtz only being detected at the probe location when the CSL is deflected, similar to what is observed in Fig. 19(b). As for vortex pairing in the CSLs, no peak is observed at $\mathrm{St_{SL}}/2$ for all probe locations. The effect is similar to what was found by Khabbouchi *et al.* [19] in the unconfined case, where strong turbulence intensity suppressed vortex pairing. Their work determined upstream turbulence contributes in two ways to this suppression. The first being turbulence breaks down Kelvin-Helmholtz vortices before merging occurs. And the second is due to the shortening of the wake, in which Kármán vortex formation interferes with shear layer breakdown. Similar observations are found for $\beta = 0.3$: The strong turbulence upstream does break down the CSLs as found by the increases in Reynolds stress there [Fig. 13(b)]. Along with earlier roll-up seen in Fig. 6(b), we conclude the blockage is sufficiently small that the effects of upstream turbulence are similar to the unconfined case.

Increasing blockage to $\beta = 0.5$, probes are again chosen to be located in the CSLs, as shown in Figs. 20(b) and 20(c). As the CSLs are found to not wander at this blockage, these points coincide with regions of maximized $\overline{u'u'}/U_b^2$. The first point considered is located at $(x/D, y/D) = (0.46, \pm 0.55)$, close to the point of separation. We observe that slight undulations occur in the instantaneous field for both CSLs at this point, indicating the formation of Kelvin-Helmholtz vortices. The energy spectrum at this point is shown by the black curve in Fig. 20(a). As expected, we find the most energetic frequency to be $\mathrm{St}_K = 0.52$, but also observed is a slight peak at a Strouhal number of $\mathrm{St_{SL}} \approx 2.8$, which is attributed to the shear layer frequency. Comparison with the LUC case of Ooi *et al.* [28] finds similar results. More precisely, they were able to observe multiple peaks in the streamwise velocity spectra, with two corresponding to the vortex shedding frequency and its first harmonic and two additional peaks at $\mathrm{St} \approx 2.1$ and 2.8. (1.4 and 1.9, respectively). Ooi *et al.* [28] were also able to supplement these findings with linear stability analysis of a mixing layer, finding a frequency of $\mathrm{St_{ML}} = 3.49$ (2.325), suggesting the larger frequency corresponds to the shear layer frequency. The similarities between the shear layer frequencies for TUCs and LUCs

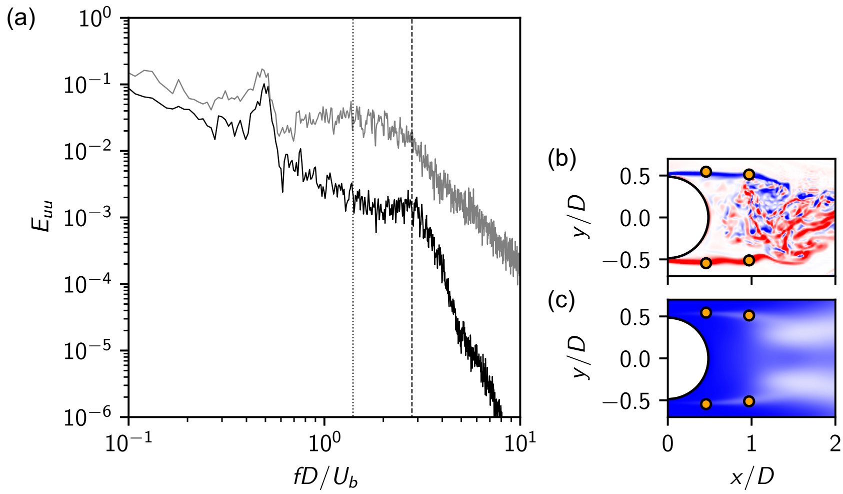

FIG. 20. Energy spectra (a) of streamwise velocity at $(x/D, y/D) = (0.46, \pm 0.55)$ (——) and $(x/D, y/D) = (0.97, \pm 0.51)$ (——) for $\beta = 0.5$. Dashed (- - - -) and dotted (......) lines denote $\mathrm{St_{SL}}$ and $\mathrm{St_{SL}}/2$, respectively. Visualization of probe locations in (b) instantaneous spanwise vorticity $\omega_z D/U_b$ and (c) streamwise normal Reynolds stress $\overline{u'u'}/U_b^2$ fields.

does contrast results from $\beta = 0.3$, which we may attribute to modifications made to the upstream profiles. For LUCs, the profile is parabolic leading to greater mass flow near the centerline, while with TUCs, the upstream profile is a canonical turbulent channel flow, with a much flatter profile. These differences are reflected in flow profiles through the gap, although we observe larger variation for $\beta = 0.3$ compared with $\beta = 0.5$ [Figs. 10(a) and 10(b)]. Assuming that mixing layer theory holds, the shear layer frequency scales with $\mathrm{St_{SL}} \sim D/\theta$, where θ is the momentum thickness. Since θ is dependent on flow profiles, the differences at $\beta = 0.3$ between both sets of upstream conditions are likely to result in the observed changes to $\mathrm{St_{SL}}$. However, for $\beta = 0.5$, the similarities cause the frequencies to remain relatively close for LUCs and TUCs. It would also be remiss to not mention the effects of turbulence, Khabbouchi *et al.* [19] found for an unconfined cylinder increases in free stream turbulence intensity also resulted in slight increases to $\mathrm{St_{SL}}$. As turbulent structures upstream were found to survive past the gap for $\beta = 0.3$, this effect may also contribute to the observed increase in $\mathrm{St_{SL}}$. While, for $\beta = 0.5$, turbulence intensity is significantly reduced through the gap, leading to a weaker effect. Moving further downstream to $(x/D, y/D) = (0.97, \pm 0.51)$, the spectrum is given by the gray curve in Fig. 20(a). The shear layer peak is no longer visible, but there does appear to be a shift towards a broadbanded bump at lower frequencies. The wide range of frequencies associated with this peak is likely caused by the breakdown of the CSL at this point due to interaction with the surviving upstream turbulent structures. Demarcated by the dotted line is the subharmonic frequency $\mathrm{St_{SL}}/2$ of the shear layer peak. We find that the local maxima of this bump is located approximately at $\mathrm{St_{SL}}/2$, which suggests the presence of vortex merging in the wake. However, the weak nature of the peak may indicate the event is infrequent.

At $\beta = 0.7$, no vortex shedding is observed, enabling vortex breakdown and merging to occur without hindrance. We therefore probe the flow within the shear layers, where the largest values of $\overline{u'u'}$ and $\overline{v'v'}$ are found (Figs. 12 and 15, respectively). Spectra of the streamwise velocity traces at different probe locations are presented in Fig. 21(a). We find for the probe closest to the cylinder $(x/D, y/D) = (0.8, \pm 0.56)$, a strong peak occurs with an estimated peak frequency of $\mathrm{St_{SL}} \approx 5.7$ and is representative of the shear layer frequency. Comparison with $\mathrm{St_{SL}}$ obtained by Ooi *et al.* [28] with LUCs finds their observed values to be much smaller at $\mathrm{St_{SL}} \approx 3.3$ (2.2). However, it is worth noting that estimates obtained with mixing layer theory for LUCs yielded

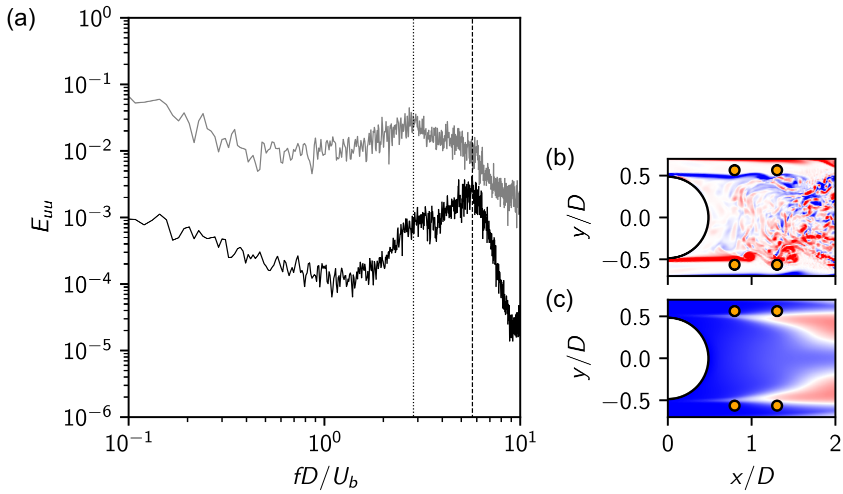

FIG. 21. Energy spectra (a) of streamwise velocity at $(x/D, y/D) = (0.80, \pm 0.56)$ (——) and $(x/D, y/D) = (1.30, \pm 0.56)$ (——) for $\beta = 0.7$. Dashed (- - - -) and dotted (……) lines denote $\mathrm{St}_{\mathrm{SL}}$ and $\mathrm{St}_{\mathrm{SL}}/2$, respectively. Visualization of probe locations in (b) instantaneous spanwise vorticity $\omega_z D/U_b$ and (c) streamwise normal Reynolds stress $\overline{u'u'}/U_b^2$ fields.

values closer to the presently obtained frequency for TUCs. It is possible that interaction between WSLs and CSLs may alter this frequency. Evidence of this may be found in Figs. 6(e) and 6(f), where, for LUCs, Kelvin–Helmholtz vortices are formed synchronously within WSLs and CSLs, whereas, with TUCs, breakdown occurs within the CSLs before the WSLs, which themselves break down further downstream. Observing now the behavior at lower frequencies, we find a bump in the streamwise spectra near the subharmonic frequency $\mathrm{St}_{\mathrm{SL}}/2 = 2.85$, indicating the presence of vortex merging. The peak is much smaller in amplitude than the primary peak at the point $(x/D, y/D) = (0.80, \pm 0.56)$, which is expected since the CSLs are only beginning to break down, as seen in Figs. 21(b) and 21(c). Moving further downstream to $(x/D, y/D) = (1.30, \pm 0.56)$, we find there is an exchange in the energy contained within these frequencies. The subharmonic peak is much more energetic than the shear layer peak, which is almost indistinguishable at this point and results from vortex merging being the primary effect.

VI. CONCLUSIONS

Simulations of flow past a cylinder confined in a channel have been performed with fully turbulent upstream conditions for blockages of $\beta = 0.3$, 0.5, and 0.7, revealing large changes in wake dynamics. For the smallest blockage, turbulence survived through the gap, enabling earlier destabilization of CSLs and moving the point of Kármán vortex formation upstream. Hence, the time- and spanwise-averaged wake is shorter than the corresponding case with a laminar upstream flow. At $\beta = 0.5$, similar effects occur; however, due to the greater streamwise acceleration through the gap, partial relaminarization occurs, resulting in weaker turbulence downstream of the gap. In combination with the lower friction Reynolds number at this blockage, shear layer destabilization is much weaker, resulting in a similar vortex formation and thus wake length between both sets of upstream flow. Finally, for the largest blockage ratio tested, $\beta = 0.7$, a large change in wake dynamics is observed. While strong relaminarization occurs, it is not enough to kill off all turbulence and thus shear layer breakdown may be observed immediately downstream of the cylinder. The effect decouples the WSLs and CSLs and thus prevents wake bias from occurring, enabling a recovery of global symmetry and suggesting the effect occurs whenever the two shear layers are decoupled. As such, it is hypothesized that wake asymmetry is only observed for sufficiently low

Reynolds numbers with LUCs. Future work will therefore involve studying the Reynolds number effect on the wake.

The destablization of the CSLs by upstream turbulence is also reflected in the fluctuating lift coeffcient C_L' where a fourfold increase compared to a laminar upstream flow is observed. This would have a profound impact to the optimal design of VIV energy converters where high C_L' is favorable.

Analysis of flow timescales also found the vortex shedding frequency at $\beta = 0.3$ and 0.5 to be lower by approximately 35%, although it is unclear why this may be the case. While within the shear layers, energetic peaks were found corresponding to the formation of Kelvin-Helmholtz vortices. The present results find the shear layer frequency to be lower with TUCs than with LUCs at $\beta = 0.3$ but similar at $\beta = 0.5$. However, at $\beta = 0.7$, the shear layer frequency is significantly higher with TUCs than LUCs. It is hypothesized this is a result of interactions between CSLs and WSLs being stronger with LUCs than TUCs. Subharmonic peaks are also found for $\beta = 0.5$ and 0.7 with TUCs, indicating the presence of vortex merging. Such a peak is not observed at the lowest blockage ratio $\beta = 0.3$, primarily due roll-up of the CSLs before pairing can occur.

ACKNOWLEDGMENTS

This work was supported by resources provided by the Pawsey Supercomputing Centre with funding from the Australian Government and the Government of Western Australia and the University of Melbourne's Research Computing Services and the Petascale Campus Initiative. W.L. acknowledges the financial support of the Defence Science Institute (DSI) RHD Student Grant and the Faculty of Engineering and Information Technology (FEIT) write-up award.

DATA AVAILABILITY

The data that support the findings of this article are not publicly available upon publication because it is not technically feasible and/or the cost of preparing, depositing, and hosting the data would be prohibitive within the terms of this research project. The data are available from the authors upon reasonable request.

APPENDIX A: MESH CONVERGENCE

For channel flows, a number of measures are typically used to ensure that the mesh is adequate in resolving the flow. One such measure is a comparison of the mesh size to the Kolmogorov length scale $\eta = (\nu^3/\varepsilon)^{1/4}$, where ε is the instantaneous dissipation,

$$\varepsilon = \nu\left(\frac{\partial u_i'}{\partial x_j}\frac{\partial u_i'}{\partial x_j}\right). \tag{A1}$$

In this case, we use the instantaneous dissipation as it does enable for finer scales to be captured compared with the mean dissipation commonly used in the literature [44]. The flow is considered adequately resolved provided that the local mesh size is of the same order as the Kolmogorov length scale [44,67]. In Fig. 22 we plot an instantaneous snapshot of the ratio Δ/η, where $\Delta = V_m^{1/3}$ is a local length scale derived from the volume of each microelement V_m. We find for all cases $\Delta/\eta < 10$, satisfying the criterion of Zahtila *et al.* [44] for convergence of flow statistics, although note that this is slightly higher than the typically accepted criterion of approximately $\Delta/\eta = 3$ for DNS and hence may be considered slightly under-resolved.

To also evaluate resolution in the near-wall region, Δy_w^+ has also been computed in Fig. 23 which shows values of $\Delta y_w^+ < 1$ over the wake region where flow gradients are largest. Hence, the near-wall resolution is satisfactory to resolve boundary effects.

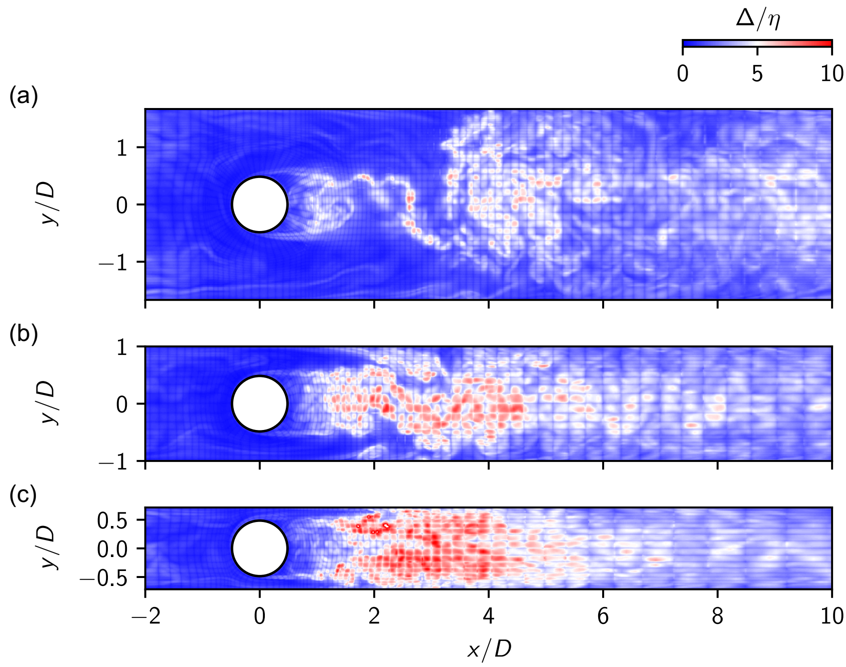

FIG. 22. Representative realizations of Δ/η for (a) $\beta = 0.3$, (b) $\beta = 0.5$, and (c) $\beta = 0.7$.

APPENDIX B: TEMPORAL WAKE BEHAVIOUR WITH TURBULENT UPSTREAM CONDITIONS

To ensure wake modulation does not occur with TUCs, we investigate wake topology in this appendix. As a measure of wake bias, we plot the crossflow velocity v/U_b along the centerplane $y/D = 0$ in Fig. 24. Beginning with LUCs, we see in Fig. 24(a) an intense band of positive v/U_b between $x/D = 2$ and 3. The bias in the wake observed in Fig. 6(e) induces a deflection in the bottom jet towards the top wall. Hence, there is a strong vertical component to the fluid velocity, which when intersecting with the centerplane results in the observed positive band. As this band extends across the span, the orientation of the wake is uniform across the span. Hence, showing a lack of wake modulation, which would instead manifest as bands of alternating sign across the span

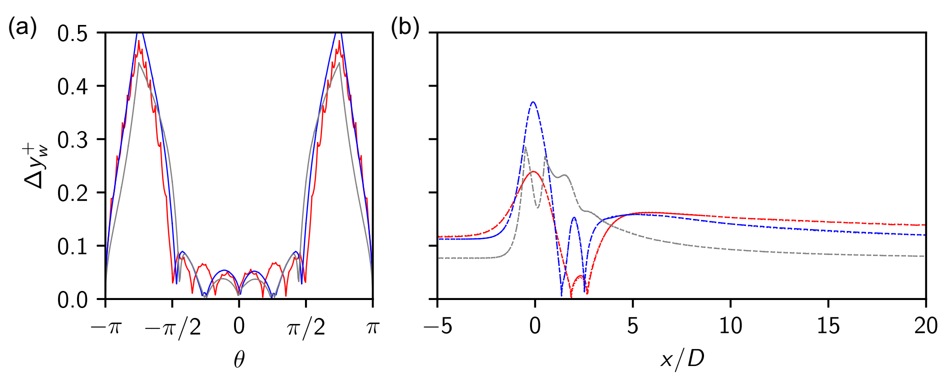

FIG. 23. Distribution of Δy_w^+ values of the first grid point for $\beta = 0.3$ (red solid line), $\beta = 0.5$ (blue solid line), and $\beta = 0.7$ (gray solid line) along the (a) cylinder surface and (b) top (……) and bottom (- - - -) channel walls.

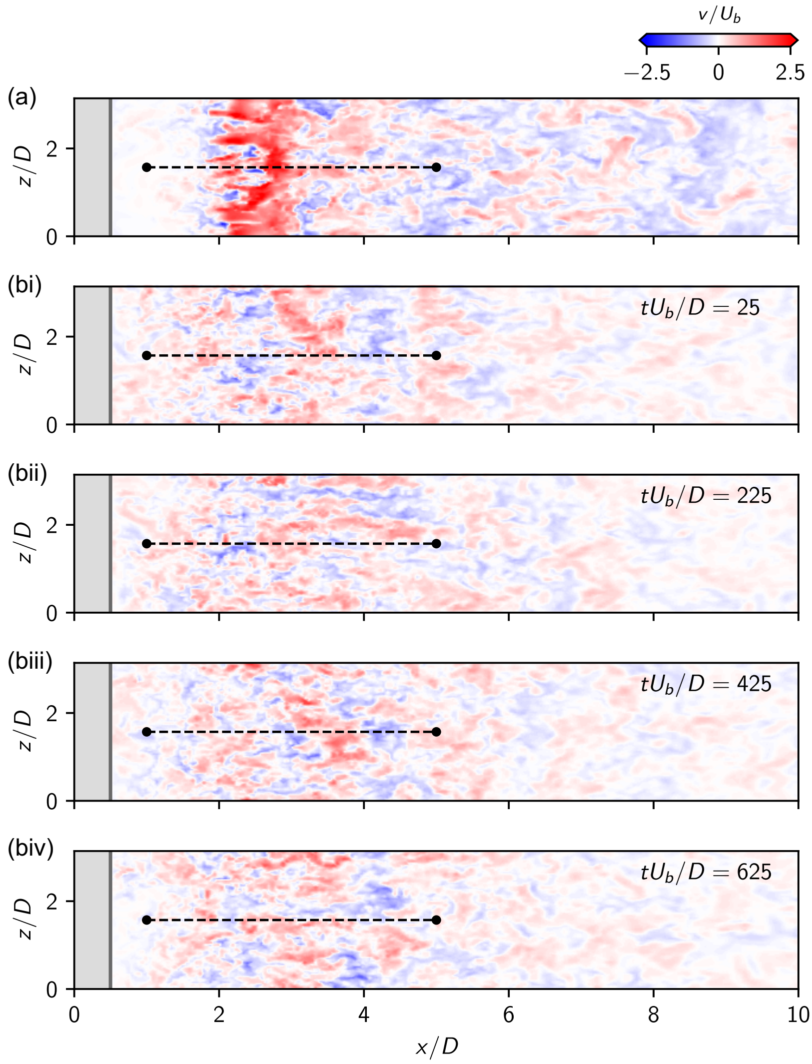

FIG. 24. Visualizations of instantaneous crossflow velocity v/U_b along the centerplane $y/D = 0$ with (a) LUCs and (b) TUCs. Slices with TUCs are visualized at various times (bi) $tU_b/D = 25$, (bii) $tU_b/D = 225$, (biii) $tU_b/D = 425$, and (biv) $tU_b/D = 425$. Dashed lines demarcate locations where spacetime diagrams are constructed in Fig. 25.

(see for example Fig. 6 of Lu *et al.* [30]). Such a result is expected as domain widths of $\mathcal{O}(10D)$ are required before the phenomena occurs [29].

Meanwhile, with TUCs, Fig. 24(b) shows there are no longer strong bands of v/U_b observed in the domain at various times. Instead, we find v/U_b is significantly weaker in magnitude, comparable to the downstream region with LUCs, and is distributed uniformly across the span. These structures are indicative of more turbulent structures, suggesting that wake bias no longer occurs. The observation may be confirmed in Fig. 6(e). Moreover, this lack of wake bias, and by extension alternating wake orientations, precludes the occurrence of instantaneous wake modulation.

To confirm these trends occur over the entire simulation interval, spacetime diagrams have previously been used to evaluate wake bias [29]. To remove short-timescale effects a low-pass filter is applied with a cutoff frequency of $f_cD/U = 0.5$, based on the peaks in Fig. 18. Spacetime

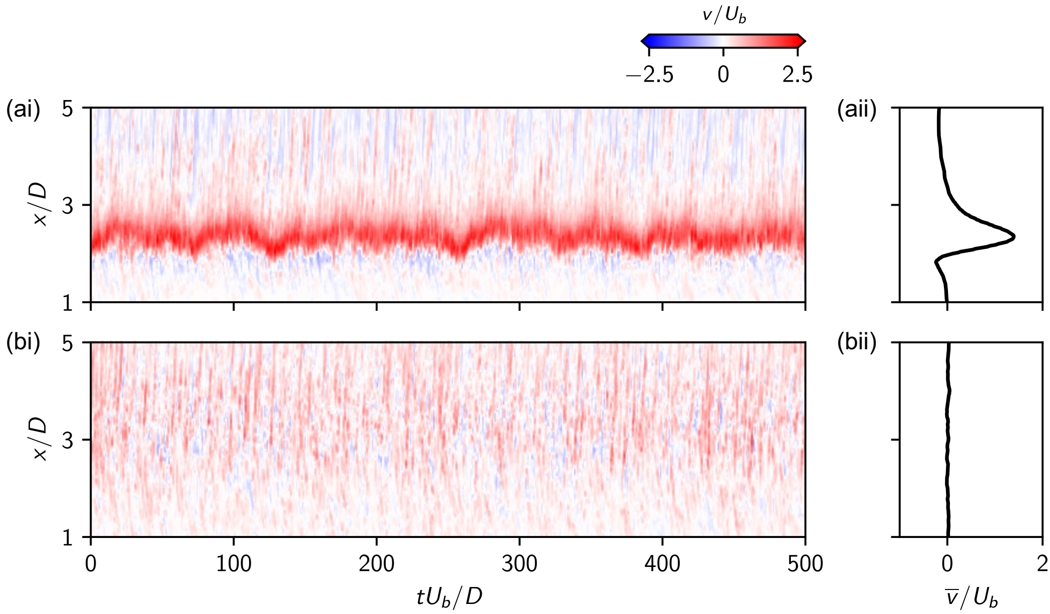

FIG. 25. Spacetime diagrams of filtered crossflow velocity along the centerline $y/D = 0$ on the midspan plane $z/D = \pi/2$, demarcated by the dashed lines in Fig. 24, with (ai) LUCs and (bi) TUCs. Temporally averaged profiles corresponding to LUCs and TUCs are depicted in (aii) and (bii), respectively.

diagrams for LUCs and TUCs are plotted in Fig. 25. The flow is sampled along the centerline, $y/D = 0$, of the midspan plane, $z/D = \pi/2$, between $x/D = 1$ and 5. With LUCs, the strong positive crossflow velocity is observed to occur over the entire simulation interval, indicative of wake bias being a persistent phenomena that results in mean wake asymmetries. Meanwhile, with TUCs, no strong crossflow velocity is observed, indicating a lack of wake bias. Hence, yielding a the temporally averaged velocity of $\overline{v}/U_b = 0$.

Results in this appendix show that unlike LUCs, which demonstrate wake bias occurring uniformly across the spanwise extent over long time intervals, TUCs result in a wake that lacks bias across the spanwise extent over long time intervals.

[1] M. M. Bernitsas, K. Raghavan, Y. Ben-Simon, and E. M. H. Garcia, VIVACE (Vortex induced vibration aquatic clean energy): A new concept in generation of clean and renewable energy from fluid flow, J. Offshore Mech. Arct. Eng. **130**, 041101 (2008).

[2] C. H. K. Williamson, Vortex dynamics in the cylinder wake, Annu. Rev. Fluid Mech. **28**, 477 (1996).

[3] J. Derakhshandeh and M. M. Alam, A review of bluff body wakes, Ocean Eng. **182**, 475 (2019).

[4] M. S. Bloor, The transition to turbulence in the wake of a circular cylinder, J. Fluid Mech. **19**, 290 (2006).

[5] J. H. Gerrard, The mechanics of the formation region of vortices behind bluff bodies, J. Fluid Mech. **25**, 401 (1966).

[6] M. F. Unal and D. Rockwell, On vortex formation from a cylinder. Part 1. The initial instability, J. Fluid Mech. **190**, 491 (1988).

[7] A. Prasad and C. H. K. Williamson, The instability of the shear layer separating from a bluff body, J. Fluid Mech. **333**, 375 (1997).

[8] O. M. Griffin and M. S. Hall, Review—Vortex shedding lock-on and flow control in bluff body wakes, J. Fluids Eng. **113**, 526 (1991).

[9] E. Konstantinidis and C. Liang, Dynamic response of a turbulent cylinder wake to sinusoidal inflow perturbations across the vortex lock-on range, Phys. Fluids **23**, 075102 (2011).

[10] J. H. Gerrard, A disturbance-sensitive Reynolds number range of the flow past a circular cylinder, J. Fluid Mech. **22**, 187 (1965).

[11] T. Maekawa and S. Mizuno, Flow around the separation point and in the near-Wake of a circular cylinder, Phys. Fluids **10**, S184 (1967).

[12] J. A. Peterka and P. D. Richardson, Effects of sound on separated flows, J. Fluid Mech. **37**, 265 (1969).

[13] C. Chyu and D. Rockwell, Evolution of patterns of streamwise vorticity in the turbulent near wake of a circular cylinder, J. Fluid Mech. **320**, 117 (1996).

[14] P. Bearman and T. Morel, Effect of free stream turbulence on the flow around bluff bodies, Prog. Aerosp. Sci. **20**, 97 (1983).

[15] D. A. Lysenko, Free stream turbulence intensity effects on the flow over a circular cylinder at $\mathrm{Re} = 3900$: Bifurcation, attractors and Lyapunov metric, Ocean Eng. **287**, 115787 (2023).

[16] L. Chan, A. Skvortsov, and A. Ooi, Turbulent flow over a mounted fence confined in a channel, in *Proceedings of the 22nd Australasian Fluid Mechanics Conference AFMC2020*, edited by H. Chanson and R. Brown (The University of Queensland, Brisbane, 2020).

[17] K. S. Kankanwadi and O. R. H. Buxton, Influence of freestream turbulence on the near-field growth of a turbulent cylinder wake: Turbulent entrainment and wake meandering, Phys. Rev. Fluids **8**, 034603 (2023).

[18] C. Norberg, Interaction between freestream turbulence and vortex shedding for a single tube in cross-flow, J. Wind Eng. Ind. Aerodyn. **23**, 501 (1986).

[19] I. Khabbouchi, H. Fellouah, M. Ferchichi, and M. S. Guellouz, Effects of free-stream turbulence and Reynolds number on the separated shear layer from a circular cylinder, J. Wind Eng. Ind. Aerodyn. **135**, 46 (2014).

[20] A. K. Soti and A. De, Vortex-induced vibrations of a confined circular cylinder for efficient flow power extraction, Phys. Fluids **32**, 033603 (2020).

[21] P. Zhang, Z. Li, T. Pan, L. Du, Q. Li, and J. Zhang, Experimental study on the lock-in of an oscillating circular cylinder confined in a plane channel, Exp. Therm Fluid Sci. **124**, 110348 (2021).

[22] J. Lin and H.-D. Yao, Modified Magnus effect and vortex modes of rotating cylinder due to interaction with free surface in two-phase flow, Phys. Fluids **35**, 123614 (2023).

[23] M. Sahin and R. G. Owens, A numerical investigation of wall effects up to high blockage ratios on two-dimensional flow past a confined circular cylinder, Phys. Fluids **16**, 1305 (2004).

[24] N. Kanaris, D. Grigoriadis, and S. Kassinos, Three dimensional flow around a circular cylinder confined in a plane channel, Phys. Fluids **23**, 064106 (2011).

[25] A. Ooi, L. Chan, D. Aljubaili, C. Mamon, J. Leontini, A. Skvortsov, P. Mathupriya, and H. Hasini, Some new characteristics of the confined flow over circular cylinders at low Reynolds numbers, Int. J. Heat Fluid Flow **86**, 108741 (2020).

[26] Q. D. Nguyen and C. Lei, Hydrodynamic characteristics of a confined circular cylinder in cross-flows, Ocean Eng. **221**, 108567 (2021).

[27] Q. D. Nguyen and C. Lei, A particle image velocimetry measurement of flow over a highly confined circular cylinder at 60% blockage ratio, Phys. Fluids **33**, 104111 (2021).

[28] A. Ooi, W. Lu, L. Chan, Y. Cao, J. Leontini, and A. Skvortsov, Turbulent flow over a cylinder confined in a channel at $\mathrm{Re} = 3{,}900$, Int. J. Heat Fluid Flow **96**, 108982 (2022).

[29] W. Lu, D. Aljubaili, T. Zahtila, L. Chan, and A. Ooi, Asymmetric wakes in flows past circular cylinders confined in channels, J. Fluid Mech. **958**, A8 (2023).

[30] W. Lu, Q. D. Nguyen, L. Chan, C. Lei, and A. Ooi, Flows past cylinders confined within ducts. Effects of the duct width, Int. J. Heat Fluid Flow **104**, 109208 (2023).

[31] Q. D. Nguyen and C. Lei, A PIV study of blockage ratio effects on flow over a confined circular cylinder at low Reynolds numbers, Exp. Fluids **64**, 10 (2023).

[32] W. Lu, L. Chan, and A. Ooi, Spectral analysis of confined cylinder wakes, Fluids **10**, 84 (2025).

[33] W. Lu, T. Zahtila, L. Chan, Q. D. Nguyen, C. Lei, G. Iaccarino, and A. Ooi, Modeling of uncertainties from spanwise asymmetries in upstream conditions and measurement plane location for flow past a circular cylinder confined within a duct, Phys. Rev. Fluids **10**, 064601 (2025).
[34] Q. D. Nguyen, W. Lu, L. Chan, A. Ooi, and C. Lei, A state-of-the-art review of flows past confined circular cylinders, Phys. Fluids **35**, 071301 (2023).
[35] M. Hiwada and I. Mabuchi, Flow behavior and heat transfer around a circular cylinder at high blockage ratios, Heat Transf. Japan. Res. **10**, 17 (1982).
[36] Q. D. Nguyen and C. Lei, Resonance in the flow past a highly confined circular cylinder, Phys. Fluids **34**, 084110 (2022).
[37] P. Fischer, S. Kerkemeier, M. Min, Y.-H. Lan, M. Phillips, T. Rathnayake, E. Merzari, A. Tomboulides, A. Karakus, N. Chalmers, and T. Warburton, NekRS, a GPU-accelerated spectral element Navier–Stokes solver, Parallel Comput. **114**, 102982 (2022).
[38] T. Zahtila, L. Chan, A. Ooi, and J. Philip, Particle transport in a turbulent pipe flow: Direct numerical simulations, phenomenological modelling and physical mechanisms, J. Fluid Mech. **957**, A1 (2023).
[39] T. Zahtila, L. Chan, A. Ooi, K. Liu, M. Benjamin, and G. Iaccarino, Influence of Miura-origami shapes on drag in turbulent flows, in *Center for Turbulence Research Proceedings of the Summer Programme* (Stanford University, Center for Turbulence Research, Stanford, CA, 2022).
[40] W. Lu, A. Ooi, L. Thomas, T. Zahtila, and G. Iaccarino, Application of multi-fidelity methods to prediction of gravity currents for uncertainty quantification, in *Proceedings of the 2024 Center for Turbulence Research Summer Program* (Stanford University, Center for Turbulence Research, Stanford, CA, 2024).
[41] P. F. Fischer, J. W. Lottes, and S. G. Kerkemeier, Nek5000 web page, https://nek5000.mcs.anl.gov/.
[42] A. Roccon, G. Amati, L. Brandt, D. Calhoun, P. Costa, W. Lu, S. Pirozzoli, D. Richter, M. Umair, D. You, T. Zahtila, and C. Marchioli, GPU-accelerated simulations of turbulence: Review of current applications and future perspectives, Phys. Rev. Fluids **11**, 034905 (2026).
[43] Y. Maday, A. T. Patera, and E. M. Rønquist, An operator-integration-factor splitting method for time-dependent problems: Application to incompressible fluid flow, J. Sci. Comput. **5**, 263 (1990).
[44] T. Zahtila, W. Lu, L. Chan, and A. Ooi, A systematic study of the grid requirements for a spectral element method solver, Computers Fluids **251**, 105745 (2023).
[45] S. Dong, G. Karniadakis, and C. Chryssostomidis, A robust and accurate outflow boundary condition for incompressible flow simulations on severely-truncated unbounded domains, J. Comput. Phys. **261**, 83 (2014).
[46] T. S. Lund, X. Wu, and K. D. Squires, Generation of turbulent inflow data for spatially-developing boundary layer simulations, J. Comput. Phys. **140**, 233 (1998).
[47] A. H. Herbst, P. Schlatter, and D. S. Henningson, Simulations of turbulent flow in a plane asymmetric diffuser, Flow, Turbul. Combust. **79**, 275 (2007).
[48] P. Schlatter and R. Örlü, Turbulent boundary layers at moderate Reynolds numbers: Inflow length and tripping effects, J. Fluid Mech. **710**, 5 (2012).
[49] R. B. Dean, Reynolds number dependence of skin friction and other bulk flow variables in two-dimensional rectangular duct flow, J. Fluids Eng. **100**, 215 (1978).
[50] B. Song, H. Ping, H. Zhu, D. Zhou, Y. Bao, Y. Cao, and Z. Han, Direct numerical simulation of flow over a cylinder immersed in the grid-generated turbulence, Phys. Fluids **34**, 015109 (2022).
[51] D. Aljubaili, L. Chan, W. Lu, and A. Ooi, Numerical investigations of the wake behind a confined flat plate, Int. J. Heat Fluid Flow **94**, 108924 (2022).
[52] E. Achenbach, Distribution of local pressure and skin friction around a circular cylinder in cross-flow up to $\mathrm{Re} = 5 \times 10^6$, J. Fluid Mech. **34**, 625 (1968).
[53] M. C. Thompson and K. Hourigan, The shear-layer instability of a circular cylinder wake, Phys. Fluids **17**, 021702 (2005).
[54] I. Afgan, Y. Kahil, S. Benhamadouche, and P. Sagaut, Large eddy simulation of the flow around single and two side-by-side cylinders at subcritical Reynolds numbers, Phys. Fluids **23**, 075101 (2011).
[55] M. Grandemange, M. Gohlke, and O. Cadot, Turbulent wake past a three-dimensional blunt body. Part 1. Global modes and bi-stability, J. Fluid Mech. **722**, 51 (2013).

[56] M. Grandemange, M. Gohlke, and O. Cadot, Bi-stability in the turbulent wake past parallelepiped bodies with various aspect ratios and wall effects, Phys. Fluids **25**, 095103 (2013).
[57] K. He, G. Minelli, J. Wang, T. Dong, G. Gao, and S. Krajnović, Numerical investigation of the wake bi-stability behind a notchback Ahmed body, J. Fluid Mech. **926**, A36 (2021).
[58] L. D. Longa, O. Evstafyeva, and A. S. Morgans, Simulations of the bi-modal wake past three-dimensional blunt bluff bodies, J. Fluid Mech. **866**, 791 (2019).
[59] A. G. Kravchenko and P. Moin, Numerical studies of flow over a circular cylinder at $Re_D = 3900$, Phys. Fluids **12**, 403 (2000).
[60] P. Parnaudeau, J. Carlier, D. Heitz, and E. Lamballais, Experimental and numerical studies of the flow over a circular cylinder at Reynolds number 3900, Phys. Fluids **20**, 085101 (2008).
[61] K. Sreenivasan, Laminarescent, relaminarizing and retransitional flows, Acta Mech. **44**, 1 (1982).
[62] P. R. Bandyopadhyay and A. Hussain, The coupling between scales in shear flows, Phys. Fluids **27**, 2221 (1984).
[63] R. Mathis, N. Hutchins, and I. Marusic, Large-scale amplitude modulation of the small-scale structures in turbulent boundary layers, J. Fluid Mech. **628**, 311 (2009).
[64] P. A. Monkewitz, The absolute and convective nature of instability in two-dimensional wakes at low Reynolds numbers, Phys. Fluids **31**, 999 (1988).
[65] S. Rajagopalan and R. A. Antonia, Flow around a circular cylinder—Structure of the near wake shear layer, Exp. Fluids **38**, 393 (2005).
[66] C. Brun, S. Aubrun, T. Goossens, and P. Ravier, Coherent structures and their frequency signature in the separated shear layer on the sides of a square cylinder, Flow Turbul. Combust. **81**, 97 (2008).
[67] P. Moin and K. Mahesh, Direct numerical simulation: A tool in turbulence research, Annu. Rev. Fluid Mech. **30**, 539 (1998).